THESIS FOR THE DEGREE OF DOCTOR OF PHILOSOPHY
IN
THERMO AND FLUID DYNAMICS

Oxy-Fuel Combustion Combined Cycles for Carbon Capture

EGILL MARON THORBERGSSON

Department of Applied Mechanics
Division of Fluid Dynamics
CHALMERS UNIVERSITY OF TECHNOLOGY

Göteborg, Sweden 2015

Oxy-Fuel Combustion Combined Cycles for Carbon Capture
EGILL MARON THORBERGSSON
ISBN 978-91-7597-167-4

Doktorsavhandlingar vid Chalmers tekniska högskola
Ny serie nr. 3848
ISSN 0346-718X
Department of Applied Mechanics
Division of Fluid Dynamics
Chalmers University of Technology
SE-412 96 Göteborg
Sweden
Telephone: +46 (0)31-772 1000

Cover:
Artistic rendering by J. Taylor

Chalmers Reproservice
Göteborg, Sweden 2015

Oxy-Fuel Combustion Combined Cycles for Carbon Capture
Thesis for the degree of Doctor of Philosophy in Thermo and Fluid Dynamics
EGILL MARON THORBERGSSON
Department of Applied Mechanics
Division of Fluid Dynamics
Chalmers University of Technology

Abstract

A short and medium term method to decrease carbon dioxide emissions is carbon capture and storage. This method captures carbon dioxide from point sources of emissions and then stores the carbon dioxide in geological formations. The aim of this thesis is to analyse and compare two different types of combined cycles that are well suited for carbon capture and storage. The cycles are the Graz cycle and the Semi Closed Oxy-fuel Combustion Cycle (SCOC-CC). The power output of the cycles analysed here is around 100 MW, which is in the mid-size power output range. The two cycles are compared to a conventional cycle that has a net efficiency of 56%. Two different layouts of the Graz cycle have been compared in this thesis. The first is a more advanced layout that incorporates a second bottoming cycle, which utilizes the heat of condensation from the flue gas condenser. The second layout is a simplified version of the Graz cycle that does not incorporate the second bottoming cycle, and is as such more comparable to the layout of both a conventional combined cycle and the SCOC-CC. The more advanced Graz cycle has around 48% net efficiency, while the simplified Graz cycle and the SCOC-CC has around 46.2% efficiency.

Another aim was to develop tools that are able to design the gas turbines that are used in oxy-fuel combustion cycles. The combustion products are mainly steam and carbon dioxide. This influences the properties of the working media in the gas turbines used in the cycles. Traditional design tools for the gas turbine therefore need modification. The thesis describes the conceptual design tool used to design the compressor part of the gas turbines. The tool is based on a one dimensional model that uses empirical data to compute losses. The thesis also describes the development of a two dimensional compressor design method.

The Graz cycle has a high water content while the SCOC-CC has a high carbon dioxide content. This difference in the working fluid will result in the turbomachinery being smaller for the Graz cycle compared to the SCOC-CC. A twin-shaft gas turbine was concluded to be better suited than a one shaft for the two oxy-fuel combustion cycles. However, the first stage of the power turbine needs to be cooled.

Keywords: Carbon capture and storage, oxy-fuel combustion combined cycles, Graz cycle, Semi-closed Oxy-fuel Combustion Combined Cycle, conceptual compressor design

Acknowledgements

My deepest gratitude goes to my supervisor Tomas Grönstedt, first for giving me the opportunity to become a Ph.D. student and second for all the fruitful discussions about the world of gas turbines; he has helped me to bring this thesis to a higher level.

My colleagues at Lund University, Magnus Genrup and Majed Sammak, get special thanks for all the discussions and collaborations that we have had during the project.

Mats Annerfeldt, Sven Axelsson, Thomas Widgren, and Adrian Dahlquist at Siemens Industrial Turbomachinery in Finspang are greatly acknowledged for the time spent at Siemens in the spring of 2013. In addition, a special thank you to Sven, for all the discussions about the design of axial compressors.

I would also like to thank all of the members, former and current, of the Turbopower process group for all the discussions about our projects and the comments received during the steering committee meetings.

My colleagues and friends at the Division of Fluid Dynamics receive my warm gratitude for making it a pleasure to show up at work. Special thanks to all the members of the Turbomachinery group at Chalmers. An extra special thanks goes to Lars Ellbrant for the interesting discussions about compressor design and to Eysteinn, Haukur and Ragnar for all the coffee breaks, lunch breaks and lunch exercises during this time at Chalmers. I would also like to thank Mikael Öhman for taking the time to create and provide the Latex template for the thesis. Further, the administrative support of Ulla Lindberg-Thieme and Monica Vargman is gratefully acknowledged.

Finally I want to give a shout-out to my wife Sigríður and my precious daughter Anna Ísafold. You can always make me laugh, even when I don't want to smile.

This research has been funded by the Swedish Energy Agency, Siemens Industrial Turbomachinery AB, GKN Aerospace, and the Royal Institute of Technology through the Swedish research program TURBOPOWER. The support of which is gratefully acknowledged.

The financial grant from Landsvirkjun's Energy Research Fund is gratefully acknowledged.

Nomenclature

Abbreviations

ASU	Air Separation Unit
CCS	Carbon Capture and Storage
GHG	Greenhouse Gas
HRSG	Heat Recovery Steam Generator
IPCC	Intergovernmental Panel on Climate Change
SCOC-CC	Semi-closed Oxy-fuel Combustion Combined Cycle

Latin symbols

A_g	cross sectional area of the hot gas path
A_b	blade area
$A_{1,..,8}$	coefficients used in polynomial for specific heat
b	axial blade chord
b	solidity exponent
c	absolute speed
c	blade chord
C_p	specific heat capacity at constant pressure
D_{eq}	equivalent diffusion factor
DF	diffusion factor
$(K_\delta)_{sh}$	correction coefficient in the deviation correlation for a blade shape with a thickness distribution different from that of the 65-series blade
$(K_\delta)_t$	correction coefficient in the deviation correlation for maximum blade thickness other than 10%
$(K_i)_{sh}$	correction coefficient in the incidence correlation for a blade shape with a thickness distribution different from that of the 65-series blades.
$(K_i)_t$	correction coefficient in the incidence correlation for maximum blade thickness other than 10%
h	enthalpy
h	height of blade
i	incidence angle
$(i_0)_{10}$	variation of zero-camber incidence angle for the 10%-thick 65-series thickness distribution
M	Mach number
$\dot{m}$	mass flow
m^*	dimensionless mass flow
m	coefficient for camber and space/chord ratio
m, m_1, m_2	coefficients used in the deviation angle correlation
m	meridional direction
n	stream surface normal direction
n	slope of the incidence-angle variation

l	computing station direction
o	minimum distance between blades (throat)
p	pressure
Pr	Prandtl number
PR	pressure ratio
R	Gas constant for the working fluid
R	degree of reaction or gas constant
r	coordinate in radial direction, radius
r_{rms}	root mean square radius
Re	Reynolds number
s	blade pitch
s	entropy
S	loss coefficient for turbines
St	Stanton number
t	blade thickness
T	temperature
T_{ci}	temperature of the cooling flow at the inlet
T_{ce}	temperature of the cooling flow at the exit
T_{bu}	uniform turbine blade temperature
TET	Turbine Entry Temperature
U	blade velocity
U_g	gas flow velocity
$\dot{W}_x$	shaft work
w	relative velocity
x	coordinate in axial direction

Greek symbols

α	absolute flow angle
α_g	convective heat transfer coefficient on the hot gas side
β	relative flow angle
$\gamma = \frac{C_p}{C_v}$	ratio between specific heats
γ	angle between the computing station direction and the radial direction
δ	deviation angle
$(\delta_0)_{10}$	variation for the 10%-thick 65-series thickness distribution
ε	blade tip clearance
ε_c	cooling effectiveness
ζ	blade stagger angle
η_c	cooling efficiency
η_p	polytropic efficency
θ	blade camber angle
θ	tangential direction
κ	blade angle
λ	ratio of excess oxygen in the combustion
ρ	density

$\sigma = \frac{c}{s}$	solidity
φ	coolant mass flow ratio
ϕ	angle between the axial and the meridional direction
ψ	stage loading coefficient
ω	loss coefficient

Subscripts

0	stagnation
1	inlet, stator inlet
2	exit, stator exit, rotor inlet
3	rotor exit
c	cooling flow
ew	end wall
g	hot gas flow
in	inlet to the turbine
is	isentropic
ml	minimum loss
out	outlet of the turbine
p	profile
rel	relative with regard to blades

List of publications

This thesis consists of an extended summary and the following appended papers:

Paper I	M. Sammak, K. Jonshagen, M. Thern, M. Genrup, E. Thorbergsson, and T. Grönstedt. Conceptual Design of a Mid-Sized Semi-Closed Oxy-fuel Combustion Combined Cycle. *ASME Turbo Expo 2011: Power for Land, Sea and Air, 6-10 June* (2011)
Paper II	E. Thorbergsson and T. Grönstedt. Multicriteria Optimization of Conceptual Compressor Aerodynamic Design. *20th International Society for Airbreathing Engines* (2011)
Paper III	M. Sammak, E. Thorbergsson, T. Grönstedt, and M. Genrup. Conceptual Mean-Line Design of Single and Twin-Shaft Oxy-Fuel Gas Turbine in a Semiclosed Oxy-Fuel Combustion Combined Cycle. *Journal of Engineering for Gas Turbines and Power* 135.8 (2013), 081502
Paper IV	E. Thorbergsson, T. Grönstedt, M. Sammak, and M. Genrup. A Comparative Analysis of Two Competing Mid-Size Oxy-Fuel Combustion Cycles. *ASME Turbo Expo 2012: Power for Land, Sea and Air, 11-15 June* (2012)
Paper V	E. Thorbergsson, T. Grönstedt, and C. Robinson. "Integration of Fluid Thermodynamic and Transport Properties in Conceptual Turbomachinery Design". *Proceedings of ASME Turbo Expo 2013: Power for Land, Sea and Air. San Antonio, USA*. GT2013-95833. American Society of Mechanical Engineers. 2013
Paper VI	E. Thorbergsson and T. Grönstedt. A Thermodynamic Analysis of Two Competing Mid-Sized Oxy-Fuel Combustion Combined Cycles. *International Journal of Greenhouse Gas Control* (Under Review)

Other publications related to the thesis by the author:

Paper A	C. Järpner, A. Movaghar, E. Thorbergsson, and T. Grönstedt. "An assessment of cooled air cooling for combined cycle gas turbines". *5th International Conference on Applied Energy*. 2013

Contents

Part I

Extended Summary

1 Introduction

Humankind's thirst for energy is becoming ever harder to quench. Figure 1.1 shows the historical trend of energy use from 1965 to 2013 [8]. The total world energy use has increased steadily from $47{\cdot}10^{12}$ kWh in 1965 to $160{\cdot}10^{12}$ kWh in 2013 (shown on the right axis in Figure 1.1). The energy per capita is also shown in Figure 1.1 for the World, USA, Sweden, China, and India (shown on the left axis in Figure 1.1). The energy use per capita for the developed countries, Sweden and USA, is much higher than for the developing countries, China and India. It is highly likely that as China and India become more developed the energy use per capita will converge to the values seen in the developed countries. This is quite evident for China, where the energy per capita in 2013 was 2.6 times the value it was in the year 2000.

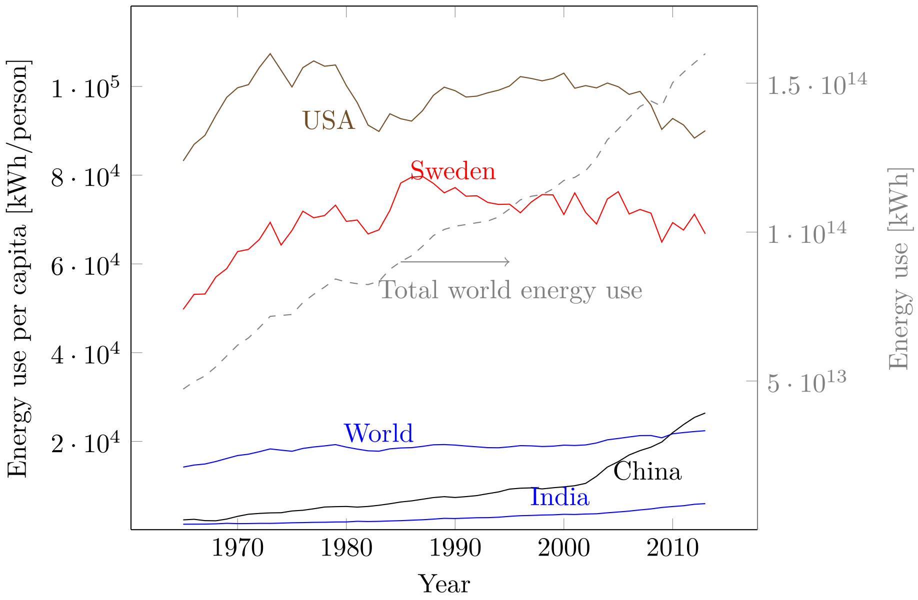

Figure 1.1: *Energy use per capita on the left axis, and total energy use on the right axis*

The largest emitter of greenhouse gas emissions (GHG) is the energy supply sector, with around 35% of the share of the total anthropogenic GHG emissions in 2010 [9]. One of the energy sector's main contributors is electricity generation, and it is expected that the demand for electricity will expand by over 70% between 2010 and 2035 [10].

It is estimated that, to keep the global temperature below the 2°C increase from pre-industrial levels, the net global GHG missions must be lowered by at least 40% and up to 70% by the year 2050. It is predicted that, if the increase in global temperature goes above 2°C, this will have an irreversible effect on the planet [9].

A number of options are available to mitigate the GHG emissions from the energy sector. These are for example energy efficiency improvements, fossil fuel switching, renewable energy, nuclear power, and carbon capture and storage (CCS). While energy efficiency improvements and fossil fuel switching have a high potential in the short term, it is the low GHG emission technologies that are needed for the long-term goal of achieving zero GHG emissions. One of the problems with low GHG renewable energies such as wind and solar is their intermittency. A solution to this problem is to use carbon capture and storage as the reserve power plants for the renewable energy technologies.

1.1 Carbon Capture and Storage

The concept behind CCS technology is to capture a relatively pure stream of carbon dioxide (CO_2) from industrial and energy related sources and store it in geological formations, in the ocean, or in mineral carbonates for long-term isolation from the atmosphere.

A number of studies have shown that, if the aim is to limit the global temperature increase resulting from climate change to 2°C, then carbon capture and storage is a critical component in the portfolio of energy technologies [11–14]. The International Energy Agency has produced a scenario, from the year 2015 to 2050, where the GHG emissions have been reduced so that the 2°C limit is achieved [11]. In the scenario, one-sixth of the CO_2 emission reductions come from the CCS in the year 2050, as compared to a business-as-usual approach. Figure 1.2 shows the scenario for the different technologies. The largest single application in the scenario is in coal and gas-fired power generation. In the year 2050 8% of all global power generation capacity, which is over 950 GW, would need to be equipped with carbon capture.

There are mainly three different approaches for capturing the CO_2 from power generation: post combustion, pre-combustion, and oxy-fuel combustion. The text that follows explains the different capturing technologies and the storage methods. The summary is based on the IPCC report Carbon Dioxide Capture and Storage [15].

1.1.1 Post Combustion Capture

As the name suggests, this method separates carbon dioxide from the flue gas after the fuel has been combusted in air. This is the combustion procedure used in nearly all fossil fuel power plants today. The post combustion system is shown in a simplified schematic in Figure 1.3. The method that is the currently preferred option for post combustion capture is a process that uses absorption, based on chemical solvents. This option has reached the commercial stage of operation.

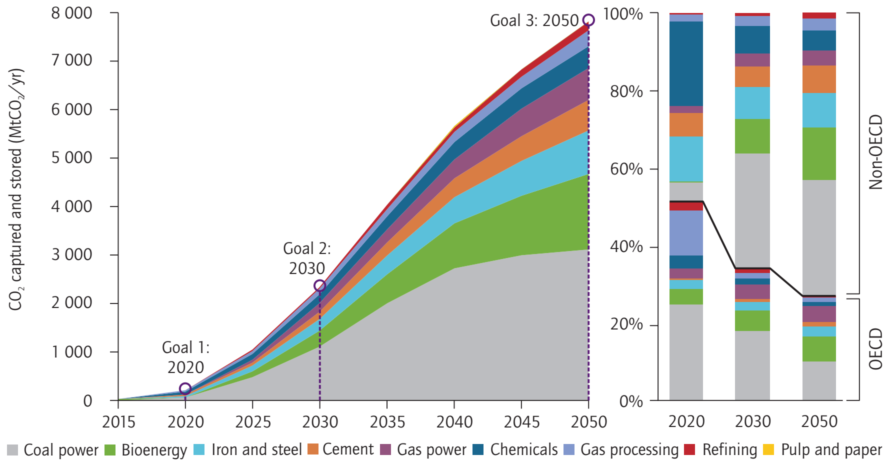

Figure 1.2: *CCS in the power and industrial sectors in the scenario proposed by International Energy Agency [11]*

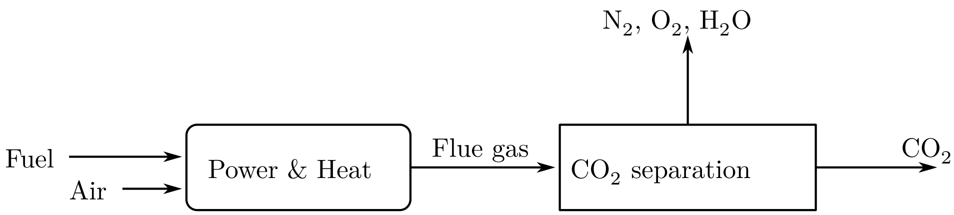

Figure 1.3: *Schematic of the post combustion capture system*

Research is being done on other methods that could be more cost effective, such as separation with membranes, solid adsorbent, or cryogenics.

One of the advantages of the post combustion capture method is that the method can be retrofitted to an existing power plant. However, since the CO_2 contents of the flue gases are quite low, or around 3% for natural gas combined cycles to around 15% for coal-fired combustion plants, the process will be quite energy intensive. The absorption process uses the reaction of an aqueous alkaline solvent to acid gas to absorb the CO_2 from the flue gas. The main energy use in the process is to heat the solvent to regenerate it and to produce steam for the stripping. The energy is also used for liquid pumping and for the flue gas fan.

The efficiency penalty of using a post combustion capture system in a power plant typically results in an efficiency drop of around ten percentage points. This number will vary depending on the percentage of CO_2 that is recovered. The recovery for post combustion is between 80% and 95%, and the exact choice for each power plant will be based on an economic trade-off.

1.1.2 Pre-combustion Capture

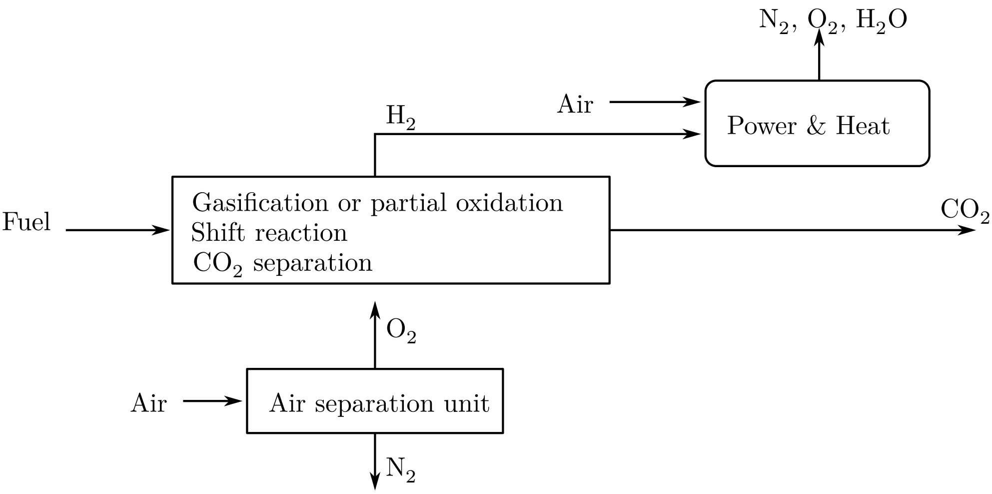

Figure 1.4: *Schematic of the pre-combustion capture system*

The pre-combustion capture method is more complex than the post-combustion method since it incorporates a greater number of processes and requires a redesign of the power plant's combustion system. A simplified schematic of the pre-combustion system is shown in Figure 1.4. The first step in the pre-combustion method is to react the fuel with either steam or oxygen, the principle is the same in both reactions, and produce a mixture of hydrogen and carbon monoxide. When the process is applied to solid fuel, it is called gasification, and, when applied to gaseous and liquid fuels, it is referred to as partial oxidation. The remaining CO is converted to CO_2 using steam in what is called a shift reaction. The CO_2 is then separated from the mixture of CO_2/H_2O. The CO_2 can now be compressed and sent to storage. Studies that have researched natural gas combined cycles using a pre-combustion method to capture the carbon dioxide indicate that the efficiency drop is around 8-14% [16, 17]. This can be compared to state of the art power plants that are based on natural gas combined cycles that have efficiencies over 60% [18].

1.1.3 Oxy-fuel Combustion Capture

The oxy-fuel combustion capture method is based on using oxygen instead of air in the combustion of the fuel. The oxygen is produced using an air separation unit. The reason is to remove nitrogen from the combustion air so that the portion of nitrogen in the flue gas becomes negligible; the flue gas will then consist mainly of CO_2 and H_2O. The separation of the mixture is then easily done by condensing the H_2O from the flue gas. The oxy-fuel combustion system is shown in a simplified schematic in Figure 1.5. One aspect of combustion of pure O_2 with the fuel is

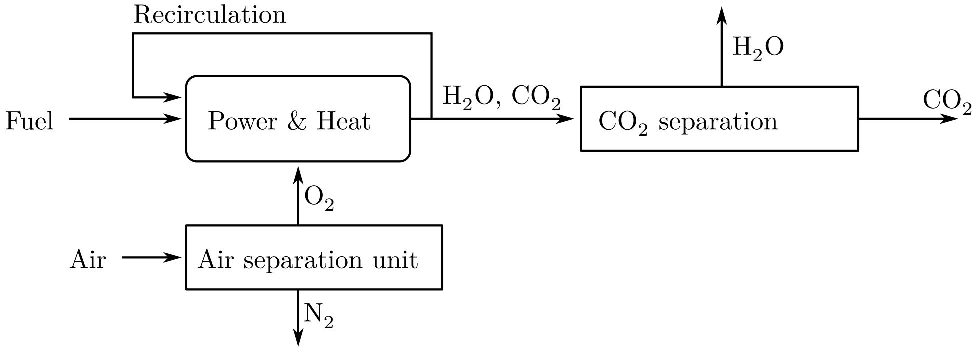

Figure 1.5: *Schematic of oxy-fuel combustion capture system*

that the flame temperature will be high, around 3500°C, which is too high for current materials used in power plants. To cool the flame temperature, flue gas can be recirculated back to the combustion chamber or other cooling media, such as H_2O, can be used to cool the combustion chamber. The air separation unit is usually cryogenic but novel technologies, such as membranes and chemical looping cycles, are being researched.

1.1.4 Storage

An important aspect of carbon capture and storage is the storage part. One of the early implementations of CCS will likely be enhanced oil recovery (EOR), where CO_2 is pumped into oil fields to improve oil recovery. The more permanent storage will likely be in a variety of geological settings in sedimentary basins. These basins include oil fields, depleted gas fields, deep coal seams and saline formations. These geological storages are illustrated in Figure 1.6. Researchers consider it likely that around 99% of the injected CO_2 will be retained for more than 1000 years.

The mechanisms that will store the CO_2 consist of trapping below an impermeable and confining layer, retention as an immobile phase being trapped into pore spaces of the storage formation, dissolution in the *in situ* formation fluids, and adsorption onto organic matter in coal and shale. Another aspect is that the CO_2 can also react with the minerals in the storage formation to produce carbonate minerals. In addition, the CO_2 will become less mobile as time passes as a result of numerous trapping mechanisms. This will further reduce the prospect of leakage.

An important factor of the storage solution part is the capacities of the storage options. Researchers have estimated that the global capacity to store CO_2 underground is large, the higher estimate is around 11 000 Gt CO_2 and the lower around 1 700 Gt CO_2. This can be compared to the carbon dioxide emissions in 2012 from the energy sector, which were 17 Gt CO_2 [9]. The capacities for different basins are shown in Table 1.1.

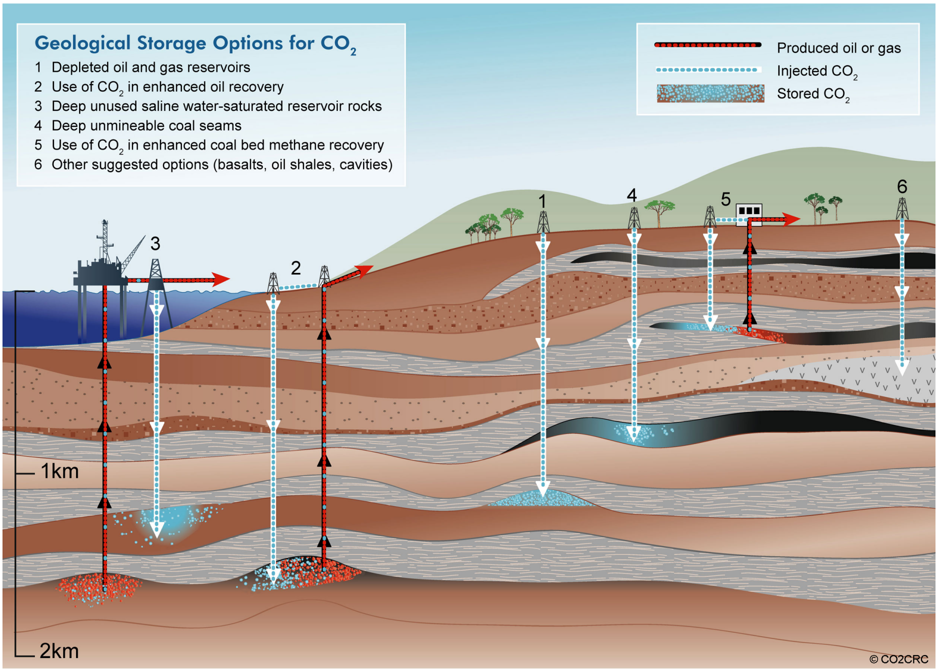

Figure 1.6: *Storage options for carbon dioxide. The options include rock formations, depleted oil and gas fields, deep saline formations and deep unmineable coal seams (courtesy of the Cooperative Research Centre for Greenhouse Gas Technologies).*

Table 1.1: *Storage capacities of different basins in Gt CO_2, both lower and higher estimates*

Basin	Lower	Higher
Depleted oil and gas reservoirs	675	900
Deep saline formations	1000	10000
Unmineable coal formations	3	200

1.2 Scope of Work - Motivation

This thesis focuses on the design of two different oxy-fuel combustion combined cycles and the conceptual design of the turbomachinery for these cycles. The two cycles are the Graz cycle and the Semi-closed Oxy-fuel Combustion Combined Cycle (SCOC-CC). The primary objective has been to compare the two cycles, both quantitatively and qualitatively, and to contribute to the understanding of the opportunities and the limitations in the design of such power plants. Another objective has been to develop tools that are able to design the gas turbine that are used in oxy-fuel combustion cycles. The major focus of this thesis has been on the compressor design. The turbine design tools and the design of the turbine for the SCOC-CC are presented in another doctoral thesis by Majed Sammak [19].

2 Oxy-fuel Combustion Combined Cycles

Oxy-fuel combined cycles represent a means to implement carbon capture for combined cycles. The basic principle of oxy-fuel combustion was introduced in section 1.1.3. Two promising implementations of the oxy-fuel combustion concept are the Semi-Closed Oxy-Fuel Combustion Combined Cycle (SCOC-CC) and the Graz Cycle. A number of studies of the thermodynamic cycles and conceptual design of the turbomachinery have been published.

Bolland and Sæther first introduced the SCOC-CC concept in 1992 where they compared new concepts for recovering CO_2 from natural gas fired power plants [20]. The basic working principle for the Graz cycle was developed by Jericha in 1985 [21]. Since then, the Graz cycle has received a considerable amount of research attention from Graz university and other universities with regard to cycle analyses and conceptual turbomachinery design [22–26]. There have also been studies that compare the cycles and the conceptual designs of the turbomachinery [27, 28].

The discussion below is based on the results given in Paper VI. This paper contains a more complete literature survey, which is only partially recapitulated in this chapter. The original analysis is extended with a sensitivity analysis of the turbine blade cooling parameters. The cycles that are studied are in the mid-size range, that is, from 30 to 150 MW [29]. Here we have aimed at keeping the gross combined power output from the cycles constant at 100 MW.

2.1 Cycle Simulation Software

The tool used to simulate the thermodynamic cycles is the heat and mass balance program, IPSEpro, developed by SimTech Simulation Technology [30]. The main part of the program uses a graphical interface where the cycle components are connected. The components are either standard models that have been implemented in the software and use simple thermodynamic equations or components that the user has modelled using more advanced equations. The connection of the components establishes a system of non-linear equations. The program uses a Newton-Raphson based strategy to solve the equation system. The first step in the solution procedure is to analyse the system of equations and determine the optimal solution procedure by breaking up the equations into small groups that can be solved successively. The next phase consists of a Newton-based gradient solver that finds a solution to the equations for each group.

2.1.1 Physical Properties

To calculate the physical properties of pure steam/water, the cycle simulation tool uses the "Industrial Formulation 1997 for the Thermodynamic Properties of Water and Steam" database [31]. The cycle simulation tool was linked to a state of the art thermodynamic and transport properties program, REFPROP, to calculate the physical properties of other fluids than pure steam and water. These fluids are carbon dioxide, nitrogen, argon, and oxygen [32–35]. The program is developed by National Institute of Standards and Technology [36] and is based on highly accurate models that are used to calculate the thermodynamic properties of pure fluids and mixtures. To calculate the thermodynamic properties of pure fluids, the program uses three models: equations of state explicit in Helmholtz energy [37], the modified Benedict-Webb-Rubin equations of state [38], and an extended corresponding states model [39]. Calculations for mixtures use a model that applies mixing rules to the Helmholtz energy of the mixture components; it uses a departure function to account for the departure from ideal mixing [40].

2.1.2 Turbine Blade Cooling Model

An important factor in analysing combined cycles is the model used to estimate the cooling requirement that is needed to cool the turbine blades. The cooling model used is the m^* model and is based on the work of Hall [41], and Holland and Thake [42]. The algorithm is based on the standard blade assumption, which assumes that the blade has infinite thermal conductivity and a uniform blade temperature. The model used in this study was originally implemented by Jordal [29].

The following is a short description of the model and the main parameters. The first parameter is the cooling efficiency, which is defined as

$$\eta_c = \frac{T_{ce} - T_{ci}}{T_{bu} - T_{ci}}, \tag{2.1}$$

where T_{ci} is the temperature of the cooling flow at the inlet, T_{ce} is the temperature of the cooling flow at the exit, and T_{bu} is the uniform blade temperature. The second parameter is the cooling effectiveness, which is defined as

$$\varepsilon_c = \frac{T_g - T_{bu}}{T_g - T_{ci}} \tag{2.2}$$

where T_g is the hot gas temperature. The model is a first-law thermodynamic, non-dimensional model, based on the dimensionless cooling mass flow parameter, which is defined as

$$\dot{m}^* = \frac{\dot{m}_c C_{p,c}}{\overline{\alpha_g} A_b} \tag{2.3}$$

where $\dot{m}_c$ is the cooling mass flow, $C_{p,c}$ is the heat capacity of the cooling fluid, α_g is the convective heat transfer coefficient on the hot gas side, and A_b is the area of the blade. The main parameter of interest is the coolant mass flow ratio

$$\varphi = \frac{\dot{m}_c}{\dot{m}_g} = \dot{m}^* \frac{C_{p,g}}{C_{p,ci}} \, \mathrm{St}_g \, \frac{A_b}{A_g} \tag{2.4}$$

where $C_{p,g}$ is the heat capacity of the hot gas, St_g is the average Stanton number of the hot gas, and A_g is the cross sectional area of the hot gas path. The Stanton number is defined as

$$\mathrm{St}_g = \frac{\alpha_g}{\rho_g U_g C_{p,g}} \tag{2.5}$$

where ρ_g is the density of the hot gas, and U_g is the flow velocity of the gas. The main output of the model is the amount of cooling mass flow, $\dot{m}_c$, needed to cool the turbine blades. To be able to calculate the mass flow, some assumptions need to be made regarding some of the parameters. The parameters that are set constant are the turbine blade temperature, T_{bu}, the Stanton number, St_g, the geometry factor, A_b/A_g, the cooling efficiency, η_c, and the turbine loss parameters, S. The values used in Paper VI are shown in Table 2.1.

Table 2.1: *Parameters assumed in the cooling model*

T_{bu}	850°C
St_g	0.005
A_b/A_g	5
η_c	0.50
S	0.2

2.1.3 Air Separation Unit

An important element in oxy-fuel combustion is the method for producing the oxygen since the procedure is quite expansive with respect to energy consumption. Different methods, such as cryogenic distillation, adsorption using multi-bed pressure swing units, and polymeric membranes, are available for separating oxygen from the air [43]. The only technology that has reached a mature technology level is cryogenic distillation. Cryogenic distillation is used today in plants that can produce up to 3000 tonnes of O_2 per day [44]. The ASU is assumed to be a cryogenic air separation plant.

The first step in the cryogenic process is to remove unwanted particles from the air, either by filters or by chemical absorption onto surfaces. The next step is to compress the air. After compression, the air is cooled to a temperature below the boiling point of oxygen. A separation column is used to separate the air into its components. Since nitrogen has a lower boiling temperature than oxygen, and the separation column has a temperature that is higher than that temperature but lower than the boiling temperature of oxygen, the oxygen will be in liquid form. The nitrogen will on the other hand be in a gaseous state. Hence, the gaseous nitrogen can be collected at the top and the liquid oxygen will stay at the bottom of the column.

The design and simulation of the air separation unit are beyond the scope of this thesis. ASU power consumption is highly dependent on the purity of the O_2 stream. It is therefore an economic trade-off between purity and cost. Typical state of the art cryogenic ASU can produce oxygen with 99.5% volume purity at a power consumption of 900 kW/(kg/s) [45]. By decreasing the purity, it is possible to reduce the power consumption of the ASU. At a purity level of 95%, the power consumption can be assumed to be around 735 kW/(kg/s) [46, 47]. The oxygen composition is shown in Table 2.2. The ASU unit delivers the O_2 stream at a

Table 2.2: *Oxygen composition*

	Mass fraction	Volumetric fraction
Ar	3.0%	2.41%
N_2	2.0%	2.29%
O_2	95.0%	95.30%

pressure of 1.2 bar and a temperature of 30 °C. An intercooled compressor, which is modelled, is used to increase the pressure of the stream to the working pressure in the combustor.

2.1.4 Other components

The expansion in an uncooled turbine is modelled using the polytropic efficiency, which is defined as

$$\mathrm{d}\,\eta_p = \frac{\mathrm{d}\,h}{\mathrm{d}\,h_{is}}\,. \tag{2.6}$$

Using the ideal gas law and the Gibbs equation and integrating from the inlet conditions to the outlet conditions, this can be extended to

$$\eta_p = \frac{(s_2 - s_1) + R\ln\left(\dfrac{p_2}{p_1}\right)}{R\ln\left(\dfrac{p_2}{p_1}\right)} \tag{2.7}$$

where R is the gas constant for the working fluid, p, s are the pressure and entropy respectively, 1 is the inlet, and 2 is the outlet of the turbine stage.

For the cooled turbine, the mixing of the coolant and the main stream gas flow result in a loss in stagnation pressure. This irreversibility is taken into account by defining a new polytropic efficiency [29, 48], defined as

$$\eta_{pr} = \eta_p - S\ \ln\left(\frac{p_{\mathrm{in}}}{p_{\mathrm{out}}}\right)\frac{p_1}{p_{\mathrm{in}} - p_{\mathrm{out}}}\frac{\dot{m}_{g,\mathrm{out}} - \dot{m}_{g,\mathrm{in}}}{\dot{m}_{g,\mathrm{in}}} \tag{2.8}$$

where p_1 is the stagnation pressure at the inlet of the rotor blade row, *in* is the inlet to the turbine and *out* is the outlet of the turbine. Parameter S is specific to each turbine and models the losses. It is typically in the range of 0.1 for a turbine that has good performance and around 0.5 for a turbine that has poor performance [49]. Dahlquist et al. examined the empirical loss models used to design turbomachinery, which are generated using air as the working fluid, and concluded that the loss models generate similar results for the working fluids in oxy-fuel cycles [50]. This indicates that it is possible to achieve the same technology level for the oxy-fuel turbines as for state of the art conventional turbines.

The compression is also modelled using the polytropic efficiency, similar to the turbine,

$$\eta_p = \frac{R \ln\left(\frac{p_2}{p_1}\right)}{(s_2 - s_1) + R \ln\left(\frac{p_2}{p_1}\right)} \tag{2.9}$$

where R is the gas constant for the working fluid, p and s are the pressure and entropy respectively, 1 is the inlet, and 2 is the outlet of the compressor.

The combustion is a simple energy model based on the assumption that all of the fuel is combusted, i.e. 100% combustion efficiency is reached. The amount of excess oxygen is calculated as

$$\lambda = \frac{\dot{m}_{\mathrm{O_2,in}}}{\dot{m}_{\mathrm{O_2,in}} - \dot{m}_{\mathrm{O_2,out}}} \tag{2.10}$$

where $\lambda = 1.0$ is stoichiometric combustion. For the oxy-fuel cycles, the combustion is nearly stoichiometric, that is $\lambda = 1.01$.

2.2 Conventional Combined Cycles

The combined cycle consists of both a gas turbine cycle and a steam cycle. A schematic of a combined cycle, with a dual pressure level steam cycle, is shown in Figure 2.1. The steam cycle utilizes the energy that is left in the exhaust gas from the gas turbine. The temperature of the exhaust gas from the gas turbine is in the range of 450°C to 600°C [51]. This high temperature exhaust gas is used in a heat recovery steam generator (HRSG) to produce the steam for a steam turbine cycle. The efficiency of the combined cycle is higher than the efficiency of either of the cycles when they are operated individually. The main application of combined cycle plants is base-load generation of electricity [51].

The working fluid in the compressor part of the gas turbine is air. The pressure ratio in the gas turbine is in the range of 15 to 35 bar. The high pressure air then goes to the combustion chamber where the fuel is combusted. The temperature of the gas that leaves the combustion chamber and enters the turbine is in the range of 1100°C to as high as 1500°C. The high temperature and pressurized flue gas is then expanded through the turbine. Next, the flue gas goes to the HRSG, which acts as the boiler for the steam cycle. After the gas has gone through the HRSG, it is exhausted into the atmosphere. The steam cycle consists of an HRSG, a steam turbine, and a condenser.

A conventional combined cycle has been modelled as a reference for the oxy-fuel combustion combined cycles. The reference cycle has a two-shaft gas turbine, i.e. gas generator and a separate power turbine. The gas generator turbine consists of two cooled stages. The cooling flows are bled from the compressor. The maximum

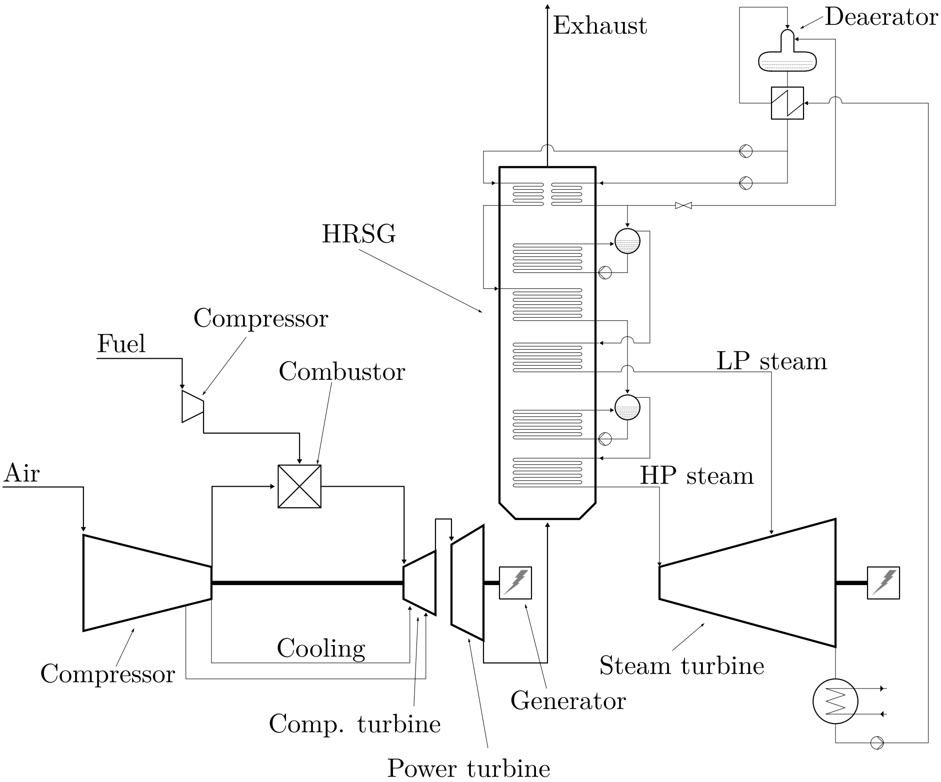

Figure 2.1: *Schematic of a combined cycle with dual pressure level steam cycle*

entry temperature for the power turbine has been set to 850 °C to eliminate the need for cooling in the power turbine. If the temperature goes above 850 °C, which is the metal temperature limit for the blades, then the first stage in the power turbine would need to be cooled. The steam cycle for a power plant in this power range usually employs single or double pressure levels and does not use reheat [52]. The design of the steam turbine has been chosen to be a single-casing non-reheat and a two pressure level steam cycle.

The HRSG shown in Figure 2.1 produces steam at two pressure levels. Hence, the HRSG consists of two steam drums, two economizers that heat up the water, two evaporators that produce steam, and two superheaters that increase the temperature of the steam. The high pressure steam was set to 140 bar and the temperature to 560 °C. The results of the cycle analysis are presented in Paper VI.

The net efficiency and the specific work for the reference cycle are shown in Figure 2.2. The specific work is the net total power divided by the inlet flow to the compressor. The pressure ratio (PR), and the turbine entry temperature (TET) are varied, while the entry temperature to the power turbine is constrained at 850°C. The maximum specific work is 545 kJ/kg, which is also the maximum

Table 2.3: *Composition of the working media in the conventional combined cycle*

	Composition [%-mass]					R	γ
	Ar	CO_2	H_2O	N_2	O_2	$\left[\frac{J}{kg\ K}\right]$	[-]
Comp. inlet	1.33	0.00	0.63	75.04	23.0	288.2	1.3984
Comp. exit	1.33	0.00	0.63	75.04	23.0	288.2	1.3529
Turb. inlet	1.30	6.49	5.72	73.27	13.22	293.2	1.2838
Turb. exit	1.30	5.34	4.82	73.59	14.95	292.3	1.3384

efficiency, 56%. The turbine entry temperature at the optimal value is $TET = 1400$ °C, and the pressure ratio is $PR = 26.2$.

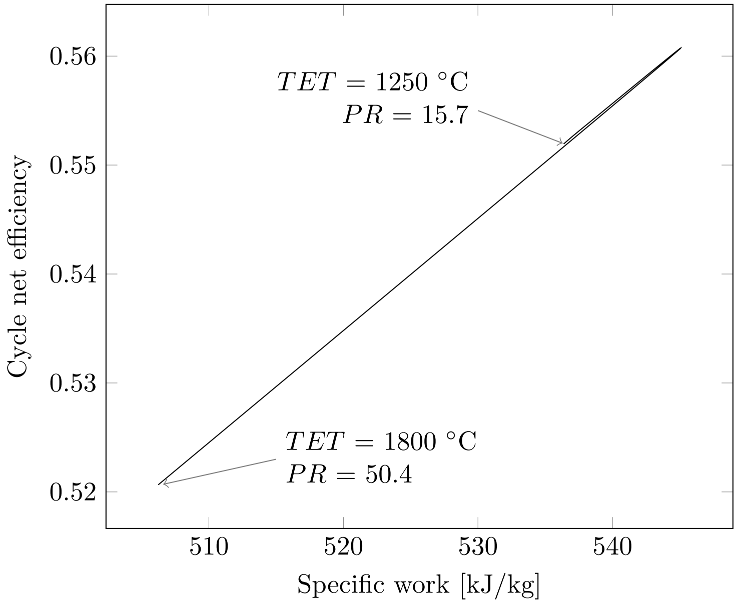

Figure 2.2: *Net efficiency and specific work for the conventional cycle*

Figure 2.3 shows the temperature and the heat flux for the heat recovery steam generator in the reference cycle. The flue gas temperature is lowered from 525°C to 96°C. The first economizer heats up both the low pressure steam and the high pressure steam, which is shown at the bottom left corner. The total energy transferred from the flue gas to the steam is around 87 MW. The composition of the working fluid in the gas turbine is shown in Table 2.3, both at the inlet and the exit of the compressor and the inlet and exit of the turbine. The main component of the working fluid in the gas turbine of the conventional combined cycle is nitrogen.

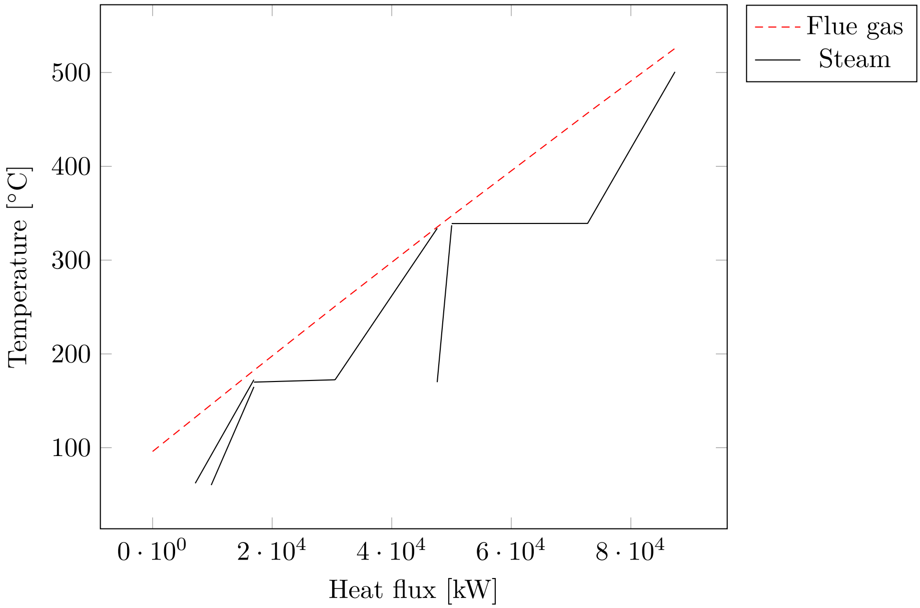

Figure 2.3: *Temperature vs. the heat flux for the HRSG in the conventional cycle*

2.3 SCOC-CC

The SCOC-CC is based on the reference cycle, and a schematic of the SCOC-CC is shown in Figure 2.4. The main layout of the SOCC-CC is quite similar to the conventional combined cycle. Now, however, the fuel is combusted with the oxygen that is produced in the ASU. The O_2 is compressed to the working pressure in the combustion chamber using an intercooled compressor. The fuel is combusted in a near to stoichiometric ratio, meaning that nearly no excess O_2 is produced. This minimizes the power demand of the ASU. The flue gas leaving the combustion chamber is mainly CO_2 and to a smaller part H_2O. The combustion products leave the combustion chamber with a temperature of 1450°C. The hot gases are then expanded in the turbine and leave the turbine with a temperature of 618°C and a pressure slightly above 1 bar. The gas turbine layout is the same as the reference cycle with a gas generator and a power turbine. The compressor turbine and the first stage in the power turbine are cooled. The cooling flow is also bled from the compressor, similar to the reference cycle. The compressor raises the pressure to 57.9 bar, and the exit temperature from the compressor is around 474°C. The composition of the working fluid at the inlet and exit of the compressor and the inlet and exit of the turbine is shown in Table 2.4. The main component of the working fluid is CO_2.

The layout of the steam cycle is unchanged from the reference cycle. It consists of an HRSG, steam turbines, a condenser, pump, and a deaerator. The units in the HRSG are the low pressure heat exchangers and the high pressure heat

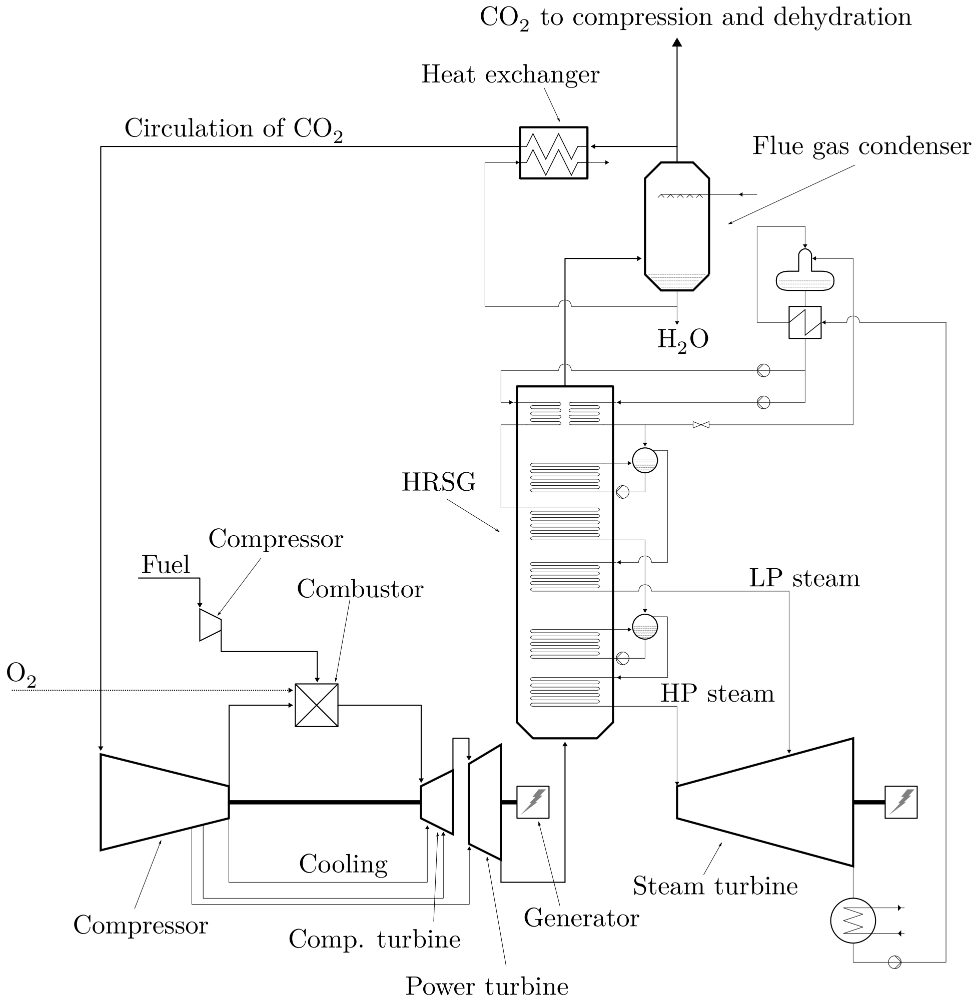

Figure 2.4: *Schematic of the SCOC-CC*

exchangers. The low pressure heat exchangers are the economizer, the evaporator, and the superheater. The high pressure heat exchangers are the same as for lower pressure: the economizer, the evaporator, and the superheater. The HRSG delivers high pressure steam with a pressure of 140 bar and a temperature of 560°C. The pressure of the low pressure steam is close to 7 bar, and the steam has a temperature of 337°C. The turbines expand the steam to a pressure of 0.045 bar and a temperature of 31°C. Figure 2.5 shows the temperature and the heat flux between the flue gas and the steam in the HRSG. It is assumed that the cooling water for the condenser has a temperature of 15°C. The total energy transferred from the flue gas to the steam is around 100 MW, which is slightly higher than for the reference cycle.

Table 2.4: *Composition of the working media in the SCOC-CC*

	Composition [%]					R	γ
	Ar	CO_2	H_2O	N_2	O_2	$\left[\frac{J}{kg\ K}\right]$	[-]
Comp.inlet	4.08	90.93	1.04	3.84	0.11	196.8	1.2953
Comp.exit	4.08	90.93	1.04	3.84	0.11	196.8	1.2055
Turb. inlet	3.84	85.58	6.86	3.62	0.11	212.3	1.1769
Turb. exit	3.90	86.96	5.36	3.67	0.11	208.3	1.2274

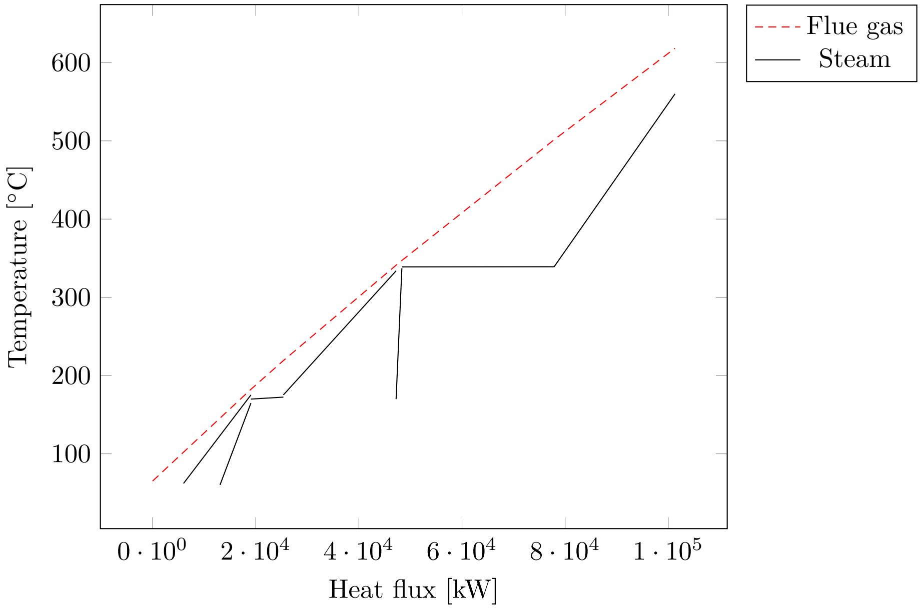

Figure 2.5: *Temperature vs. the heat flux for the HRSG in the SCOC-CC*

The flue gas leaves the HRSG with a temperature of 65°C, which is lower than in a regular dual-pressure combined cycle. The reason that the temperature is lower for the SCOC-CC is that the specific heat of the flue gas is lower than the specific heat of the flue gas in the conventional combined plant. After the HRSG, the flue gas goes through a condenser where the H_2O is condensed from the flue gas. The condenser uses water, with a temperature of 15°C, as cooling media to remove the H_2O from the flue gas. The flue gas is cooled in this process. The flue gas contains 90% carbon dioxide after the condenser. The CO_2 stream that leaves the condenser has near 100% relative humidity. This humidity can possibly condense at the entry to the compressor, which could have a deteriorating effect for the compressor. The CO_2 stream is therefore heated before it enters the compressor using the heat from the flue condensation. A major part of the carbon dioxide stream, 93%, goes back to the compressor while the rest goes to compression and dehydration, and is then transported to storage. The net efficiency and the specific work for the SCOC-CC are shown in Figure 2.6. The specific work is calculated in the same way as for the reference cycle; the net power output is divided by the inlet mass flow of the compressor. The pressure ratio (PR) increases from left to right for all the curves. The highest efficiency is 46.16% with a specific work of 518 kJ/kg. The specific work is in a similar range as for the reference cycle, with the highest being around 560 kJ/kg.

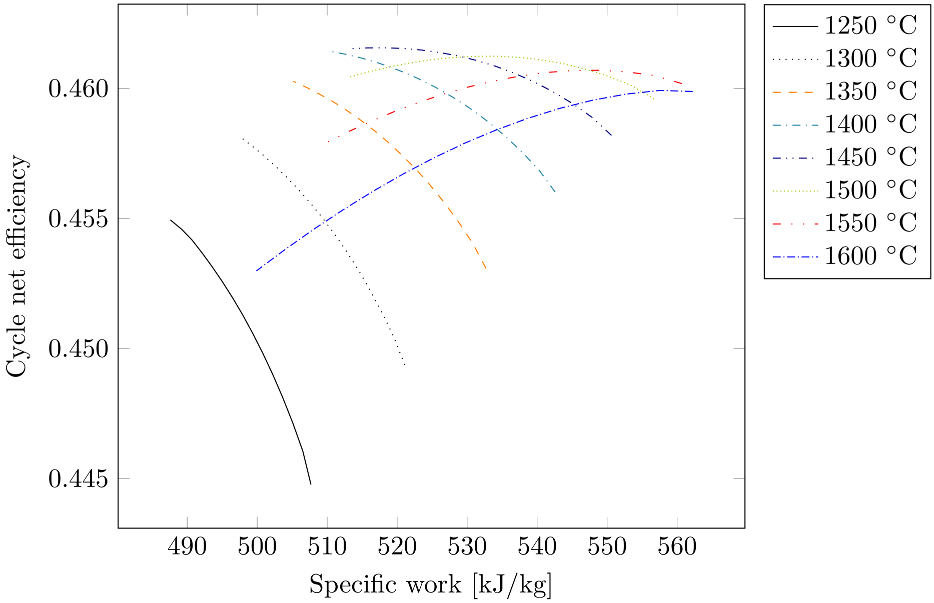

Figure 2.6: *Net efficiency and specific work for the SCOC-CC*

2.4 Graz Cycle

The Graz cycle is another concept that uses oxy-fuel in a combined cycle. The most common layout of the Graz cycle, which has been published by Graz University, incorporates two bottoming cycles. The first bottoming cycle uses a typical HRSG and a steam turbine. The steam is only expanded, however, to the pressure of the combustion chamber. This is because the steam is used for cooling, both for the combustion chamber and for the gas turbine blades. The second bottoming cycle uses the enthalpy of the condensation, and it is assumed that it is possible to expand the steam to a particularly low pressure, 0.021 bar. This cycle was modelled in Paper IV and is further examined in a later section.

2.4.1 Simplified Graz cycle

It is hard to imagine that the design of the Graz cycle will deviate so greatly from the current layout of the combined cycle, taking into account that the power industry has a high inertia regarding change. Instead it is better to use the reference cycle as a starting point in the modelling of the Graz cycle and incorporate the major design features of the Graz cycle in the reference cycle. The cycle incorporates an intercooler to reduce the temperature of the gas at the exit of the compressor as well as steam cooling. This layout, not implementing the second bottoming cycle, is viewed to be a more reasonable one as a first generation design of the cycle. It also makes the complexity level of the SCOCC-CC and the Graz cycle more comparable. The cycle illustrated in Figure 2.7 should therefore be understood as a simplified variant of the Graz cycle.

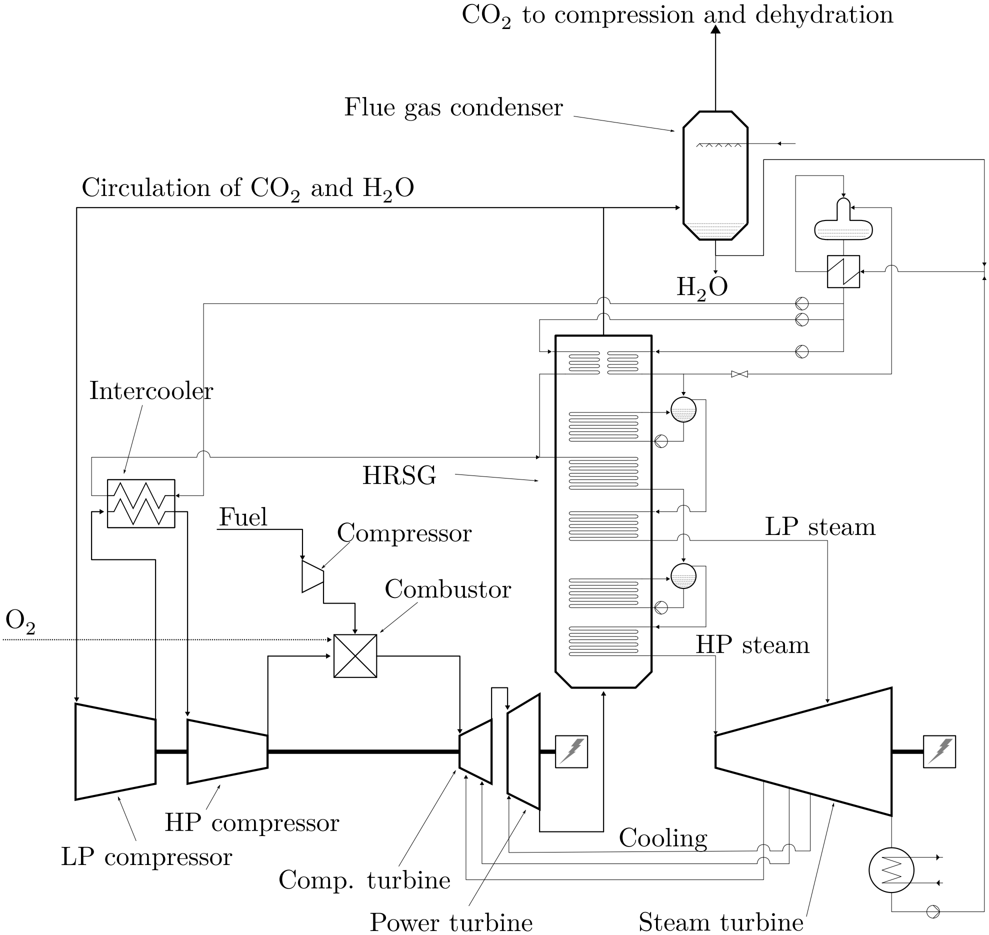

Figure 2.7: *Schematic of the Graz cycle*

Table 2.5: *Composition of the working media in the Graz cycle*

	Composition [%]					R	γ
	Ar	CO_2	H_2O	N_2	O_2	[J/(kg K)]	[-]
Comp. inlet	1.30	28.94	68.40	1.23	0.127	377.1	1.2976
Comp. exit	1.30	28.94	68.40	1.23	0.127	377.1	1.2424
Turb. inlet	1.52	33.71	63.20	1.43	0.148	363.2	1.1964
Turb. exit	1.30	28.94	68.40	1.23	0.127	377.1	1.2504

Another feature is that the flue gas is sent straight to the compressor after the HRSG without condensing the H_2O from the flue gas. Part of the flue gas is sent to a condenser where a major part of the H_2O is condensed from the flue gas; after the condenser, the flue gas is sent to the CO_2 compression and purification process. The CO_2 is afterwards transferred to the storage site.

The temperature of the gas leaving the combustion chamber is 1450°C and the pressure is 35.6 bar. The gas expands in the turbine to a pressure of 1.03 bar with a temperature of 614 °C. The gas turbine has the same layout as in the SCOC-CC; it is a two shaft with a compressor turbine and a power turbine. The compressor turbine and the first stage in the power turbine are cooled using steam from the steam cycle. The composition of the working media for the Graz cycle is shown in Table 2.5.

The energy left in the flue gas is then used in the HRSG to generate steam for the bottoming cycle. The flue gas leaves the HRSG with a temperature of 100°C. The temperature of the flue gas is limited because the gas contains water, which should not be condensed before the gas enters the compressor. Nearly 70% of the flue gas is sent to the compressor, while the remaining gas goes to the flue gas condenser. The compressor, as stated before, raises the pressure to 35.6 bar, which results in a temperature of 605°C. The temperature in the last stages of the compressor is higher than is usually encountered in industrial compressors. This indicates the need for expansive blade materials that can withstand such high temperatures.

The HRSG is a dual pressure level design, as in the reference cycle. The units in the HRSG are the low pressure heat exchangers and the high pressure heat exchangers. The low pressure heat exchangers are the economizer, the evaporator, and the superheater. The high pressure heat exchangers are the economizer, the intercooler, the evaporator, and the superheater. The high pressure steam produced in the HRSG has a pressure of 140 bar and a temperature of 559°C. This is because the pinch temperature for the superheater is 25 °C. The low pressure steam has a pressure of 7 bar and a temperature of 337°C. Figure 2.8 shows the temperature and the heat flux between the flue gas and the steam. The first part of the curves shows the heat flux for the intercooler. The heat exchangers in the HRSG come next. The total energy flow from the flue gas to the steam is around 96 MW. The steam turbine expands to a pressure of 0.045 bar. However, a large part of the steam is bled from the steam turbine and used for cooling in the gas

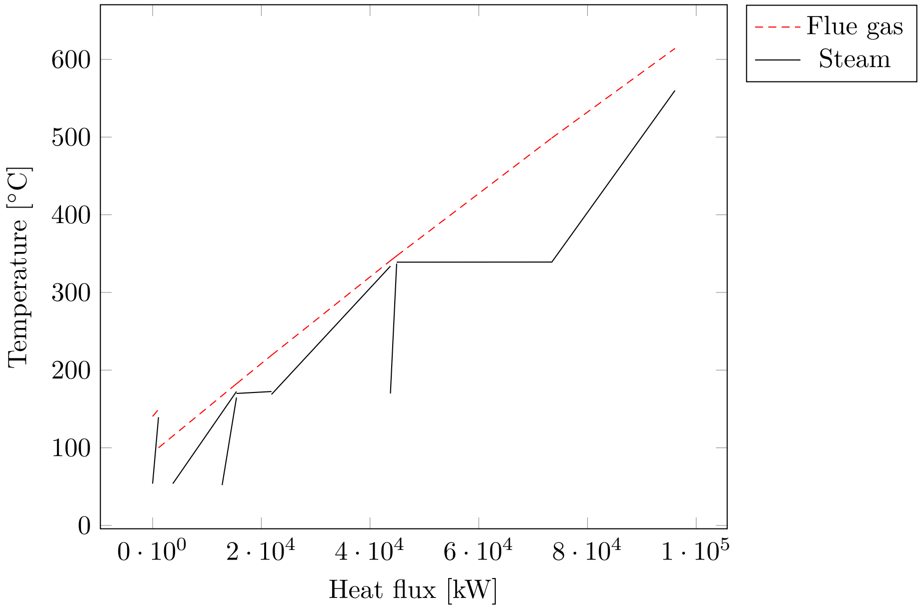

Figure 2.8: *Temperature vs. the heat flux for the HRSG in the Graz cycle*

turbine. The cooling flow needed is nearly 60% of the high pressure steam.

The net efficiency and the specific work for the Graz are shown in Figure 2.9. The specific work is calculated in the same way as for the other two cycles; the net power output is divided by the inlet mass flow to the compressor. The pressure ratio increases from right to left for all the curves. The optimal net efficiency is 46.16% which has a specific work of around 1070 kJ/kg, making it considerably higher than for both the reference cycle and the SCOC-CC.

2.4.2 Full Graz cycle

As stated earlier, the full Graz cycle incorporates two bottoming cycles. The first is a conventional steam cycle and has the same layout as in the reference cycle. The second bottoming cycle uses the heat of condensation to produce the steam. A schematic of the full Graz cycle is shown in Figure 2.10 with the second bottoming cycle, using the same layout as is in publications from Graz University (see e.g. [23]). The full Graz cycle has been examined at a turbine entry temperature of 1450 °C. As for the simplified Graz cycle, the reference cycle was used as the basis for the modelling of the full Graz cycle, i.e. all the same assumptions have been used for the topping cycle and the first bottoming cycle. The second bottoming cycle uses two compressors to increase the pressure and temperature of the flue gas. The first compressor increases the pressure to 1.25 bar and the second to 1.95 bar. The isentropic efficiency of the compressors is assumed to be 85% and the isentropic efficiency of the steam turbine is assumed

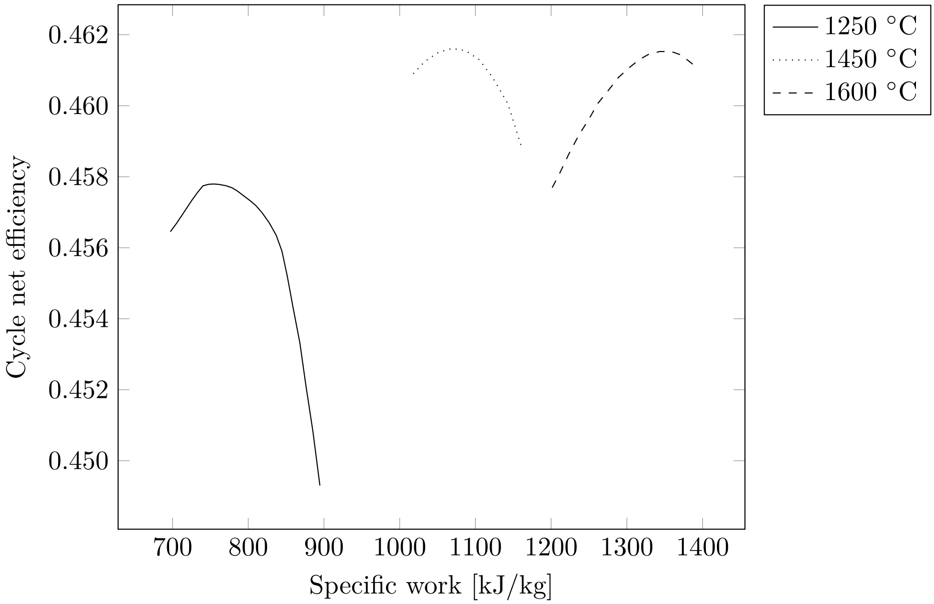

Figure 2.9: *Net efficiency and specific work for the Graz cycle*

to be 86%. The dew point temperature of the flue gas is around 100 °C at the inlet of the flue gas condenser. This puts a constraint on the steam cycle since the cooling flow to the condenser needs to have a lower temperature than the dew point temperature. The first flue gas condenser is the evaporator in the steam cycle. To be able to produce steam with such a low temperature, the pressure needs to be sub-atmospheric, or around 0.42 bar. The second bottoming cycle is able to produce an additional 3 MW, taking into account the power needed for both compressors. Another assumption used in the publications from the Graz University is the condenser pressure for the steam cycles. They have assumed 0.021 bar, while in Paper VI it was assumed to be 0.045 bar.

Results for both condenser pressures are shown in Figure 2.11. The second bottoming cycle increases the net efficiency of the Graz cycle to above 48%, when using a condenser pressure of 0.045 bar. This is an increase of close to 2% compared to the results of Paper VI. If it is further assumed that it is possible to condense to a pressure of 0.021 bar, the net efficiency is increases to above 49.4%, which is an increase of more than 3% compared to the results of Paper VI.

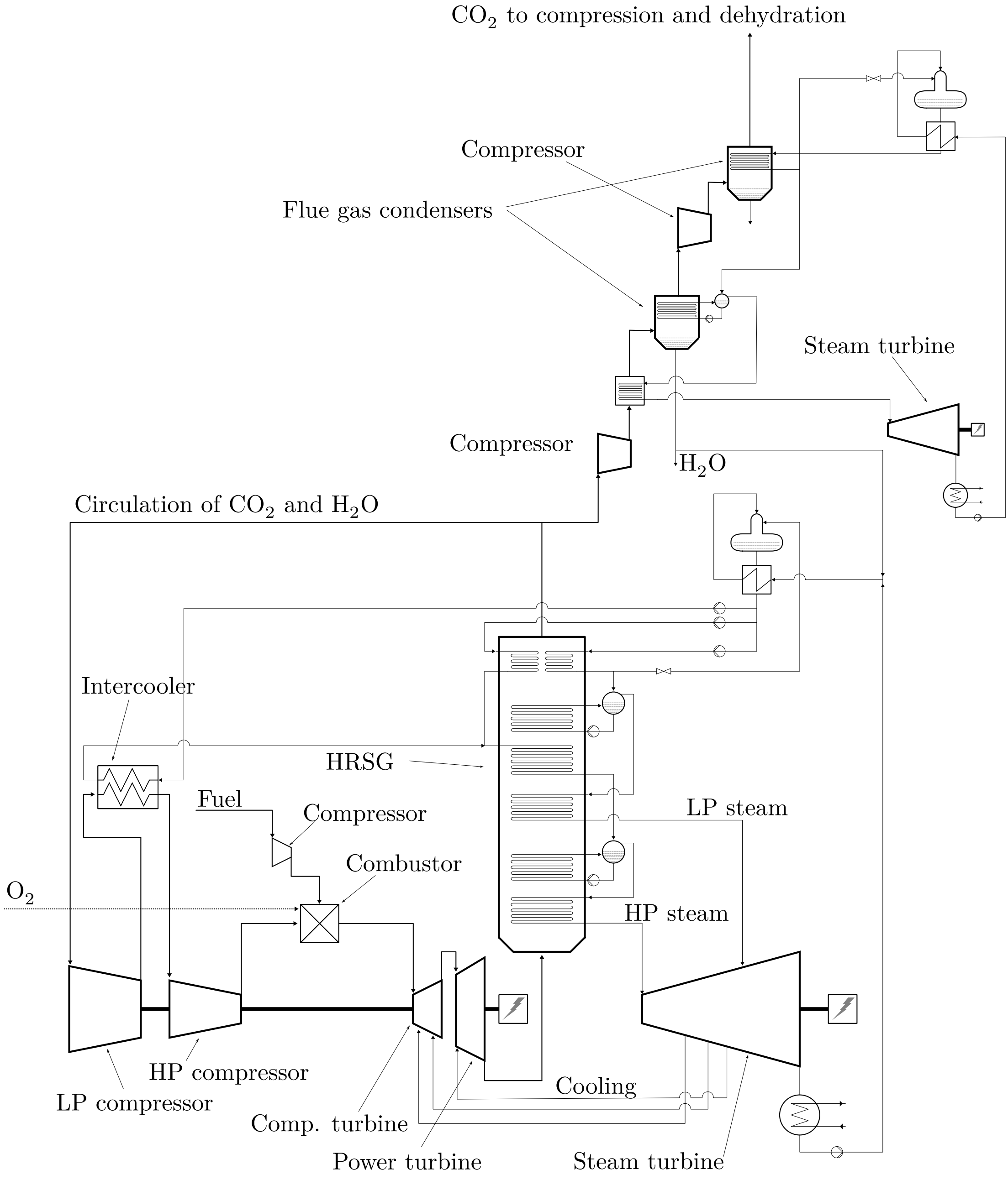

Figure 2.10: *Schematic of the full Graz cycle*

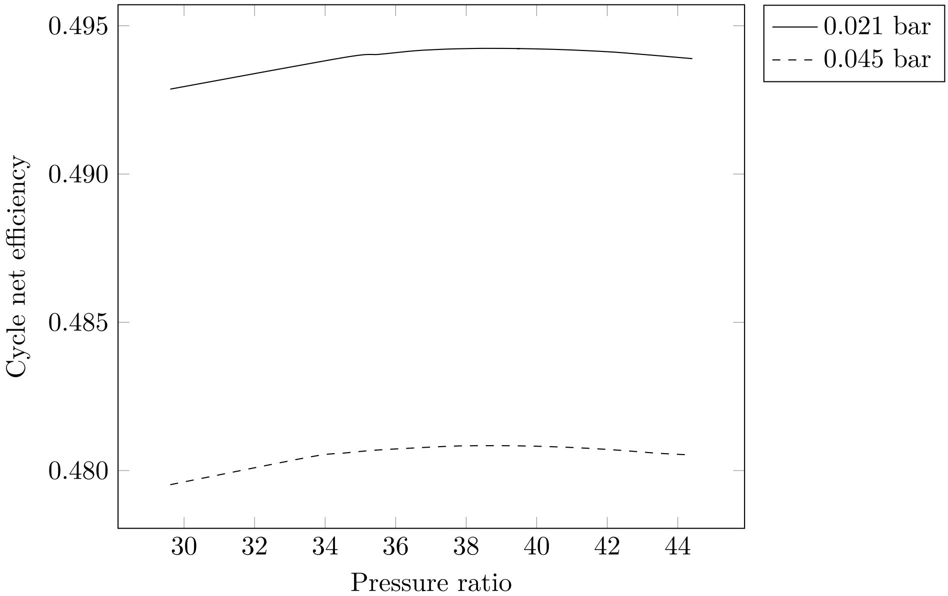

Figure 2.11: *Net efficiency as a function of the pressure ratio and the condenser pressure for the full Graz cycle at a turbine entry temperature of 1450 °C*

2.5 Sensitivity Analysis

2.5.1 Stanton number

A sensitivity analysis was made for the Stanton number. Louis [53] formulated an empirical rule to calculate the Stanton number for convective heat transfer on the hot side of a gas turbine blade

$$\mathrm{St}_g = 0.5\ \mathrm{Re}_g^{-0.37}\ \mathrm{Pr}_g^{-2/3} \tag{2.11}$$

where Re_g and Pr_g are the Reynolds number and Prandtl number respectively. The Stanton number was calculated for three different fluids, dry air, CO_2, and H_2O, at low temperature and pressure, and high temperature and pressure. The Reynolds number was computed with an assumed chord length of 75 mm and velocity of 100 m/s. The results are shown in Table 2.6. The Stanton number for the CO_2 is lower than the Stanton number for air, while it is higher for H_2O. The difference between the working fluids is comparatively small, however. The Stanton number also shows the same trend when the temperature and pressure are increased. It is evident that the Stanton number of CO_2 is lower than that of air, and the Stanton number of H_2O is higher as compared to air. The assumptions here are that the velocity and the length of the blade are constant for all cases. It is highly unlikely that the blade chord length and velocity will be the same for all three cycles since the speed of sound, and the specific work, are dissimilar

Table 2.6: *Sensitivity analysis of the Stanton number*

T °C	P bar	Fluid	Pr	ν cm^2/s	Re	St_g
1250	10	Air	0.74	0.249	$0.3 \cdot 10^6$	0.0057
1250	10	CO_2	0.72	0.158	$0.5 \cdot 10^6$	0.0050
1250	10	H_2O	0.87	0.398	$0.2 \cdot 10^6$	0.0061
1250	40	Air	0.74	0.063	$1.2 \cdot 10^6$	0.0034
1250	40	CO_2	0.72	0.040	$1.9 \cdot 10^6$	0.0030
1250	40	H_2O	0.86	0.100	$0.8 \cdot 10^6$	0.0037
1600	10	Air	0.74	0.351	$0.2 \cdot 10^6$	0.0065
1600	10	CO_2	0.71	0.221	$0.3 \cdot 10^6$	0.0056
1600	10	H_2O	0.85	0.588	$0.1 \cdot 10^6$	0.0072
1600	40	Air	0.74	0.088	$0.8 \cdot 10^6$	0.0039
1600	40	CO_2	0.71	0.056	$1.3 \cdot 10^6$	0.0034
1600	40	H_2O	0.84	0.147	$0.5 \cdot 10^6$	0.0043

between the three working fluids in the cycles.

2.5.2 Turbine Blade Cooling Model

A sensitivity analysis was made on the parameters used in the turbine blade cooling model. The cooling flow is a difficult process to model, especially in a simple thermodynamic analysis, while it has a large impact on the results. To be able to predict the flow, a large number of assumptions have to be made regarding the parameters used in the model. This introduces considerable uncertainty in the predicted cycle results, particularly since the cooling media is different between all three cycles. This introduces the question of whether it is possible to use the same values for all the three cycles in the cooling model, as has been done in the cycle analysis. This sensitivity analysis was accomplished by varying the main parameters used in the cooling models to see how they influence the main results of the cycle analysis. The main parameters are the Stanton number, St, the turbine blade temperature, T_{bu}, the geometry factor, A_b/A_g, the cooling efficiency, η_c, and the loss parameter, S. The original values used for the cooling flow parameters are shown in Table 2.1.

The change in the cooling flow ratio, ϕ, and the net efficiency of the cycles with respect to the parameters used in the model are shown in Table 2.7, along with the optimal values from Paper VI. Relative change from the optimal values is shown in parentheses.

The cooling of the blades improves when the Stanton number is decreased, resulting in a lower cooling flow requirement, which in return results in a higher net efficiency. The opposite happens when the Stanton number is increased; the cooling flow increases, and the efficiency decreases. When taking into account

Table 2.7: *Sensitivity analysis for the turbine blade cooling model. Relative changes from the optimal values are shown in the parenthesis.*

Cycle	Variable	ϕ	Efficiency
Reference		0.216	56.0
SCOC-CC	Optimal values	0.346	46.2
Graz		0.170	46.2
Reference	$\mathrm{St}_g = 0.004$ (-20%)	0.178 (-19.1%)	56.9 (1.5%)
SCOC-CC	$\mathrm{St}_g = 0.004$ (-20%)	0.296 (-15.4%)	47.0 (1.8%)
Graz	$\mathrm{St}_g = 0.004$ (-20%)	0.139 (-18.1%)	47.3 (2.4%)
Reference	$\mathrm{St}_g = 0.006$ (20%)	0.247 (12.1%)	55.4 (-1.2%)
SCOC-CC	$\mathrm{St}_g = 0.006$ (20%)	0.390 (11.5%)	45.4 (-1.6%)
Graz	$\mathrm{St}_g = 0.006$ (20%)	0.198 (16.6%)	45.1 (-2.4%)
Reference	$T_{bu} = 800$ °C (-5.9%)	0.276 (25.4%)	54.7 (-2.4%)
SCOC-CC	$T_{bu} = 800$ °C (-5.9%)	0.427 (21.9%)	44.8 (-3.0%)
Graz	$T_{bu} = 800$ °C (-5.9%)	0.211 (24.1%)	44.6 (-3.4%)
Reference	$T_{bu} = 900$ °C (5.9%)	0.169 (-23.3%)	57.1 (1.9%)
SCOC-CC	$T_{bu} = 900$ °C (5.9%)	0.280 (-20.1%)	47.3 (2.4%)
Graz	$T_{bu} = 900$ °C (5.9%)	0.136 (-20.3%)	47.4 (2.7%)
Reference	$A_b/A_g = 4$ (-20%)	0.178 (-19.1%)	56.9 (1.5%)
SCOC-CC	$A_b/A_g = 4$ (-20%)	0.296 (-15.4%)	47.0 (1.8%)
Graz	$A_b/A_g = 4$ (-20%)	0.139 (-18.1%)	47.3 (2.4%)
Reference	$A_b/A_g = 6$ (20%)	0.251 (14.3%)	55.3 (-1.4%)
SCOC-CC	$A_b/A_g = 6$ (20%)	0.390 (11.5%)	45.4 (-1.6%)
Graz	$A_b/A_g = 6$ (20%)	0.198 (16.6%)	45.1 (-2.4%)
Reference	$\eta_c = 0.40$ (-20%)	0.260 (18.2%)	55.1 (-1.7%)
SCOC-CC	$\eta_c = 0.40$ (-20%)	0.401 (14.6%)	45.2 (-2.0%)
Graz	$\eta_c = 0.40$ (-20%)	0.205 (20.6%)	44.8 (-2.9%)
Reference	$\eta_c = 0.60$ (20%)	0.184 (-16.2%)	56.7 (1.2%)
SCOC-CC	$\eta_c = 0.60$ (20%)	0.305 (-12.9%)	46.8 (1.5%)
Graz	$\eta_c = 0.60$ (20%)	0.145 (-15.0%)	47.1 (2.0%)
Reference	$S = 0.10$ (-50%)	0.217 (-1.5%)	56.8 (1.3%)
SCOC-CC	$S = 0.10$ (-50%)	0.348 (-0.5%)	47.3 (2.5%)
Graz	$S = 0.10$ (-50%)	0.170 (-0.2%)	46.8 (1.3%)
Reference	$S = 0.30$ (50%)	0.215 (-2.2%)	55.3 (-1.3%)
SCOC-CC	$S = 0.30$ (50%)	0.344 (-1.8%)	44.8 (-2.9%)
Graz	$S = 0.30$ (50%)	0.170 (-0.1%)	45.5 (-1.4%)

the results of the sensitivity analysis of the Stanton number in Table 2.6, and that the gas turbine for the Graz turbine will be smaller, it is evident that the Stanton number for the SCOC-CC is overestimated and the Stanton for the Graz cycle is underestimated. This indicates that the efficiency for the SCOC-CC is underestimated and for the Graz cycle overestimated.

The cooling requirement increases if the turbine blade temperature, T_{bu}, is decreased, which results in a lower net efficiency for the cycle. When the blade temperature is increased, the cooling requirement decreases, which then results in a higher net efficiency.

The geometry factor, A_b/A_g, has been varied by 20% from the set value of $A_b/A_g = 5$. If the geometry factor is reduced, it means that there is less area to be cooled compared to the cross sectional area of the gas path. This means that cooling is improved, which will result in a higher net efficiency. If the geometry factor is increased, the cooling requirement increases and the net efficiency decreases.

The cooling efficiency was varied by 20% from the fixed value, $\eta_c = 0.50$. The cooling efficiency directly relates to the cooling requirement. When the cooling efficiency is reduced, the net efficiency increases; if the cooling efficiency is increased, the net efficiency decreases.

The cooling expansion loss factor was varied by 50% from the set value, $S = 0.20$. The factor does not substantially influence the cooling mass flow. It does however influence the efficiency of the turbine expansion, which in turn affects the net cycle efficiency. If the loss factor is decreased, the net efficiency is increased and, if it is increased, the net efficiency decreases.

The results of the sensitivity analysis show that all three cycles follow the same trends when the values of the cooling model parameters are varied. The parameter that has the highest impact on the net efficiency is the blade temperature (T_{bu}). This can be assumed to be one of the parameters that will be the same between all cycles, since the material used in the blades can be assumed to be the same for all three cycles. It is possible to estimate the qualitative errors from the uncertainty of the assumption regarding the parameters used in the cooling model. As seen in Table 2.6, the Stanton number for the SCOC-CC is overestimated compared to the reference cycle, while it is underestimated for the Graz cycle. This means that the efficiency for the SCOC-CC is under-predicted while it is over-predicted for the Graz cycle. It is possible to use the specific work for the cycles to see the relation between the geometry factor for the cycles. The specific work is similar for the reference cycle and the SCOC-CC, while it is nearly double for the Graz cycle. This indicates that the gas turbine for the Graz cycle will be considerably smaller. This leads in turn to the conclusion that the geometry factor for the Graz cycle is underestimated as compared to the reference cycle and the SCOC-CC, which indicates that the efficiency of the Graz cycle is over-predicted compared to the reference cycle.

Since the Graz cycle uses steam to cool the turbine blades, which has better heat transfer characteristics than air and CO_2, it can be deduced that the cooling efficiency for the Graz cycle is underestimated. This suggests that the efficiency for the Graz cycle is under-predicted compared to the reference cycle and the SCOC-CC. The cooling expansion loss factor is dependent on the size of the turbine. As has been mentioned, it can be assumed that the Graz cycle will be smaller than the reference cycle and the SCOC-CC. This suggests that the loss factor will be higher for the Graz cycle, but it is believed to be negligible in comparison to the other parameters.

To conclude, it is suspected that only one parameter is under-predicted for the SCOC-CC, which should increase the efficiency of the cycle. For the Graz cycle, there are two parameters that introduce an over-prediction of the efficiency, while one parameter introduces an under-prediction. This indicates, qualitatively, that the SCOC-CC should have a slightly higher efficiency while the Graz cycle a slightly lower efficiency than is predicted in Paper VI.

3 Conceptual Compressor Design

The basic purpose of the compressor is to convert shaft work into increased pressure of the working fluid. In the most common configuration, the first blade row in the compressor consists of blades that guide the flow into the first rotor. This blade row is called Inlet Guide Vanes (IGV). The next two blade rows define what is called a stage. The blades in the first row rotate, and are called rotors, while the blades in the second row are stationary and are either called stators or nozzles. A typical meridional view of a compressor is shown in Figure 3.1. In both rows, the blades decelerate the local relative flow velocity and thus behave as diffusers. The possible deceleration is limited, since, if the flow is slowed down too much, it will separate from the blades and the compressor is likely to exhibit flow instabilities called stall or surge. The flow in the compressor is unsteady, three dimensional and viscous effects influence the flow in an intricate manner.

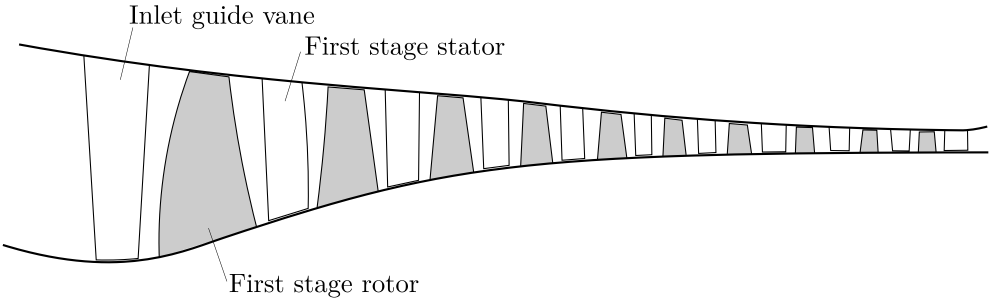

Figure 3.1: *Meridional view of a compressor*

Compressor design is an iterative process using a number of tools that come from the arsenal of engineering, such as thermodynamics, fluid dynamics, solid mechanics, manufacturing, material mechanics and structural mechanics. The conceptual design of a compressor starts with one dimensional thermo-fluid design, called mean-line design. Thereafter, a two dimensional design approach, based on inviscid flow and correlation based loss predictions, called throughflow, is frequently applied. The next step is to go to detailed three dimensional design using advanced computational fluid dynamics codes. Along with the aerodynamic design, structural dynamics and solid mechanics modelling must be performed before compressor rig design and tests can commence. There is often a need to iterate between the design stages described above to achieve a good solution for the compressor design. Even after the testing phase of the compressor has been initiated, modifications to the designs are often needed to ensure efficient and reliable operation in the entire working range.

The main losses in a compressor blade row are profile, endwall, tip leakage, and shock losses. A typical spanwise loss distribution for a high speed compressor blade row is shown in Figure 3.2.

The working fluids in the two oxy-fuel combustion cycles are very different from

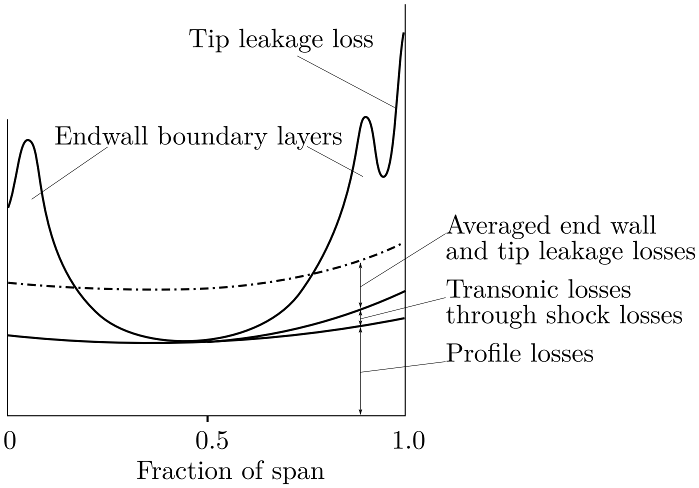

Figure 3.2: *Typical spanwise loss distribution in high speed compressors. Reproduced from [54].*

the working fluid in a conventional cycle, as can be seen in Tables 2.3, 2.4, and 2.5. The working fluid properties have large effects on the results of the performance calculations and the conceptual design results. In the cycle simulations, the fluid properties were computed using the REFPROP program, as mentioned earlier. The fluid properties are therefore accounted for at high accuracy. It is also possible to use the REFPROP program to calculate the fluid properties in the conceptual compressor design process, which is of course the most accurate way to model the fluid properties. However, this comes with one drawback; it is quite costly in terms of computational time. Another method is to assume thermally perfect gas (also called semi-perfect gas). In a thermally perfect gas, the enthalpy, h and specific heat at constant pressure, C_p, are functions of temperature only, and not pressure. Thermally perfect gas also follows the ideal gas law. It is possible to estimate the deviation from the ideal gas by using the compressibility factor, which is defined as

$$Z = \frac{p}{RT\rho} \tag{3.1}$$

where p is pressure, R is the specific gas constant, T is the temperature, and ρ is the density. It is possible to calculate the compressibility factor, for the three different working fluids, for the compression process by assuming a polytropic efficiency, here assumed to be $\eta_p = 0.90$. The compressibility factor for all three working fluids is shown in Figure 3.3 going from the initial pressure, 1 bar, to the final pressure for all three working fluids. The compression factor is nearly constant at 1 for the working fluid of the reference cycle. The working fluid for the SCOC-CC is also very close to following the ideal gas law. As expected, the working fluid for the Graz cycle deviates most from the ideal gas, as it has a high water content. However, it only deviates by 0.01, and is constant at 0.99 for the whole path. It is therefore reasonable to assume that the all three working fluids follow the ideal gas law.

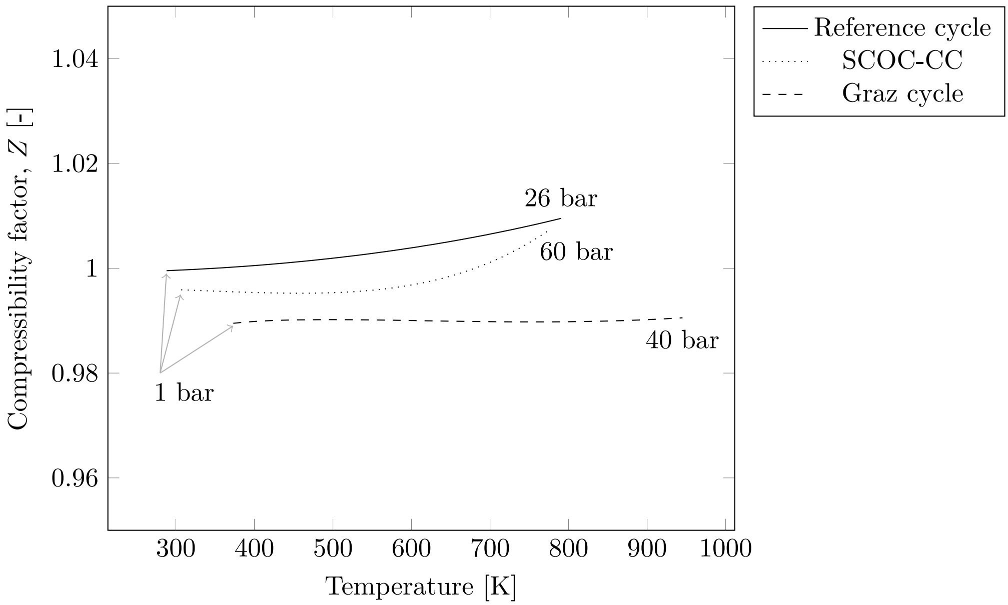

Figure 3.3: *Compressibility factor for the working fluid in the three cycles on the compression paths*

A polynomial model for the specific heat is shown in Equation 3.2 [55].

$$\begin{aligned} C_p = A_0 + A_1\left(\frac{T}{1000}\right) + A_2\left(\frac{T}{1000}\right)^2 + A_3\left(\frac{T}{1000}\right)^3 + A_4\left(\frac{T}{1000}\right)^4 \\ +A_5\left(\frac{T}{1000}\right)^5 + A_6\left(\frac{T}{1000}\right)^6 + A_7\left(\frac{T}{1000}\right)^7 + A_8\left(\frac{T}{1000}\right)^8 \end{aligned} \tag{3.2}$$

The specific heat for the working fluid in the reference cycle at both at 1 bar and 30 bar is shown in Figure 3.4. The specific heat for the SCOC-CC working fluid at 1 bar and 60 bar is shown in Figure 3.5, and the specific heat for the working fluid of the Graz cycle is shown in Figure 3.6, both at 1 bar and 40 bar.

The compression process is modelled assuming a polytropic path, and a polytropic efficiency of 90% for all three working fluids. It can be seen in Figure 3.4 that there is a slight dependency on pressure at the exit temperature of the compression process for the working fluid in the reference cycle. It is slightly larger for the SCOC-CC working fluid, as can be seen in Figure 3.5 and is quite large for the working fluid in the Graz cycle, as can be seen in Figure 3.6. This pressure dependency is taken into account in the model for the specific heat by fitting the model to the compression paths for all three working fluids, as is shown in Figures 3.4, 3.5, and 3.6. The coefficients for the three working fluids are shown in Table 3.1.

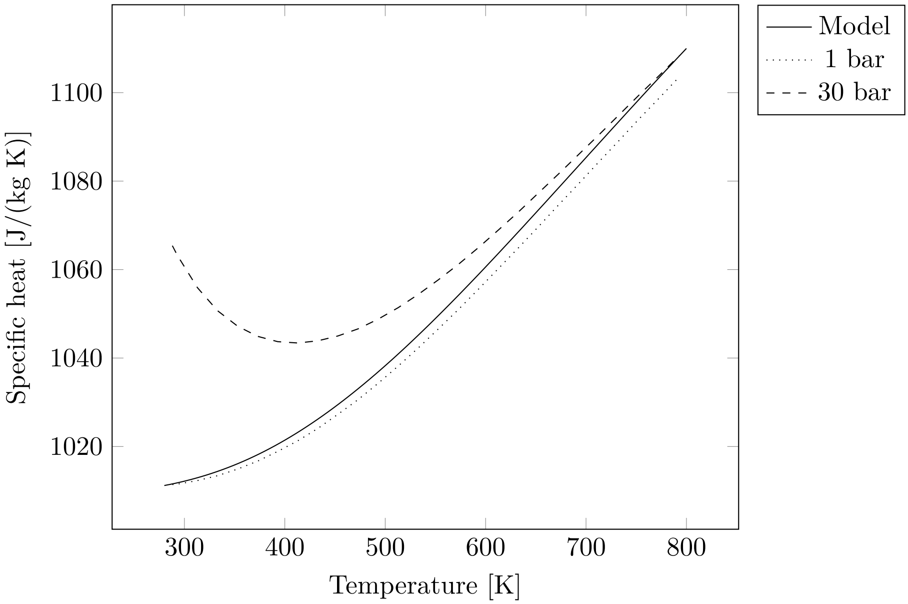

Figure 3.4: *Specific heat for the fluid composition in the reference cycle*

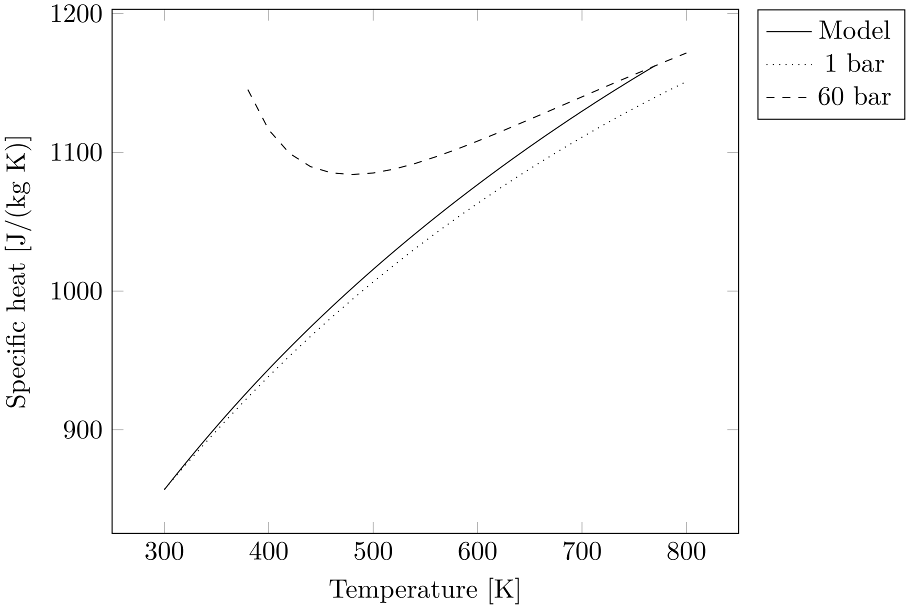

Figure 3.5: *Specific heat for the fluid composition in the SCOC-CC*

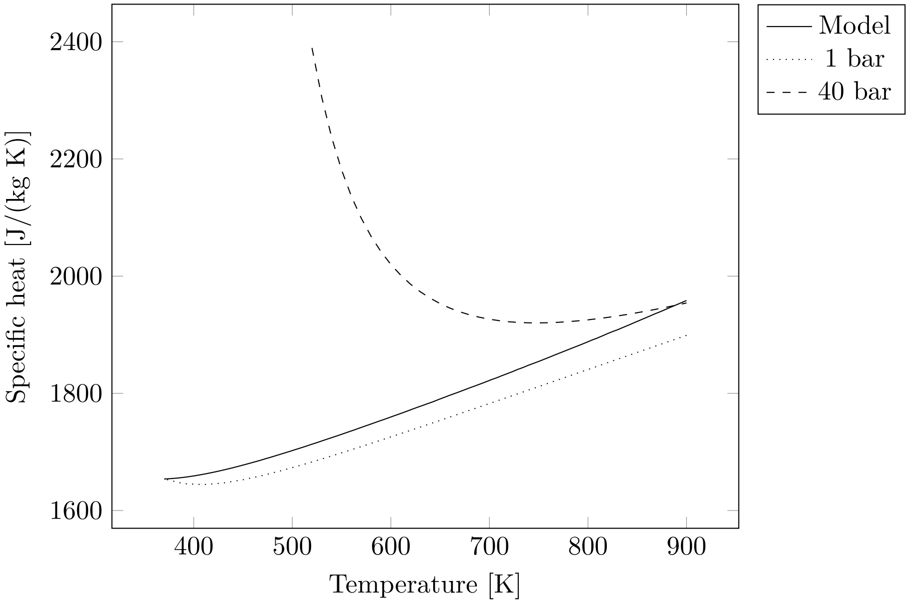

Figure 3.6: *Specific heat for the fluid composition in the Graz cycle*

Table 3.1: *Coefficients for the specific heat model*

	Reference cycle	SCOC-CC	Graz cycle
A_0	$1.007{\cdot}10^{0}$	$7.168{\cdot}10^{-1}$	$7.379{\cdot}10^{0}$
A_1	$-5.733{\cdot}10^{-2}$	$-2.095{\cdot}10^{0}$	$-6.631{\cdot}10^{1}$
A_2	$1.257{\cdot}10^{0}$	$2.301{\cdot}10^{1}$	$3.318{\cdot}10^{2}$
A_3	$-9.175{\cdot}10^{0}$	$-8.766{\cdot}10^{1}$	$-9.473{\cdot}10^{2}$
A_4	$3.271{\cdot}10^{1}$	$1.939{\cdot}10^{2}$	$1.696{\cdot}10^{3}$
A_5	$-5.992{\cdot}10^{1}$	$-2.670{\cdot}10^{2}$	$-1.943{\cdot}10^{3}$
A_6	$6.051{\cdot}10^{1}$	$2.264{\cdot}10^{2}$	$1.389{\cdot}10^{3}$
A_7	$-3.245{\cdot}10^{1}$	$-1.087{\cdot}10^{2}$	$-5.653{\cdot}10^{2}$
A_8	$7.277{\cdot}10^{0}$	$2.266{\cdot}10^{1}$	$1.003{\cdot}10^{2}$

3.1 One Dimensional Design

One dimensional design methods simplify the flow, and assume that it is steady and inviscid by considering only the variation in the flow along the root-mean-square (rms) radius through the compressor. The rms radius divides the annulus area into two equal parts, one above the rms radius, and one below. The rms radius is defined as

$$r_{rms} = \sqrt{\frac{1}{2}\left(r^2_{\text{casing}} + r^2_{\text{hub}}\right)}\,.$$

The method neglects spanwise variations and uses parameters that represent average conditions. The flow field in a compressor is a complex three dimensional system that can be modelled using computational fluid dynamics. Still, the one dimensional method provides a necessary starting point for the design based on a limited number of input parameters. It also provides a rapid convergence that can be used to explore a wide range of different compressor designs.

The one dimensional model is used to predict the flow at the mean radius, shown in Figure 3.7. A design process based on such a simplified model is called a mean-line design. The mean-line code is based on solving the mean velocity

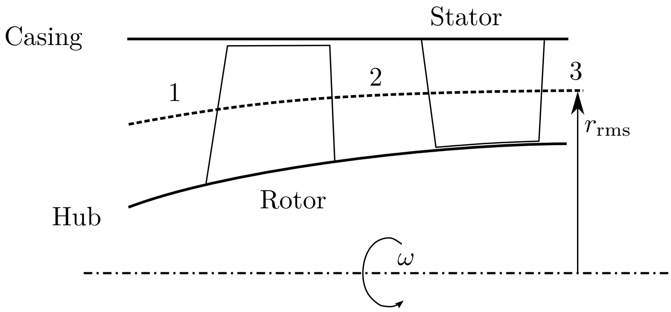

Figure 3.7: *Meridional view of a compressor stage*

triangles, shown in Figure 3.8, and using the Euler equation, Equation 3.3, to relate the enthalpy change to the velocity triangle.

$$\dot{W}_x = \dot{m}\Delta h_0 = \dot{m}(U_2 c_{\theta_2} - U_1 c_{\theta_1}) \tag{3.3}$$

Correlations are used to take viscous effects into account as part of the mean-line design. The correlations found in the open literature are generally based on traditional blade profile types such as double circular arc (DCA) or NACA. The mean-line code used herein assumes that the blades are DCA blades.

The parameters for the boundary conditions are the mass flow, the inlet temperature and pressure, and the working fluid in the compressor. The values for these parameters are received from the cycle simulation tool. Other input parameters are number of stages, rotational speed, relative tip Mach number at the rotor of the first stage, axial inlet Mach number, stage loading (Equation 3.4), degree of reaction (Equation 3.5), aspect ratio of the blades, the geometry of each stage such as constant hub radius, constant mean radius, or constant casing radius, the ratio of the clearance between the blade and the casing and the blade chords.

$$\psi = \frac{\Delta h_0}{U^2} \tag{3.4}$$

$$R = \frac{\text{static enthalpy rise in the rotor}}{\text{static enthalpy rise in the stage}} \tag{3.5}$$

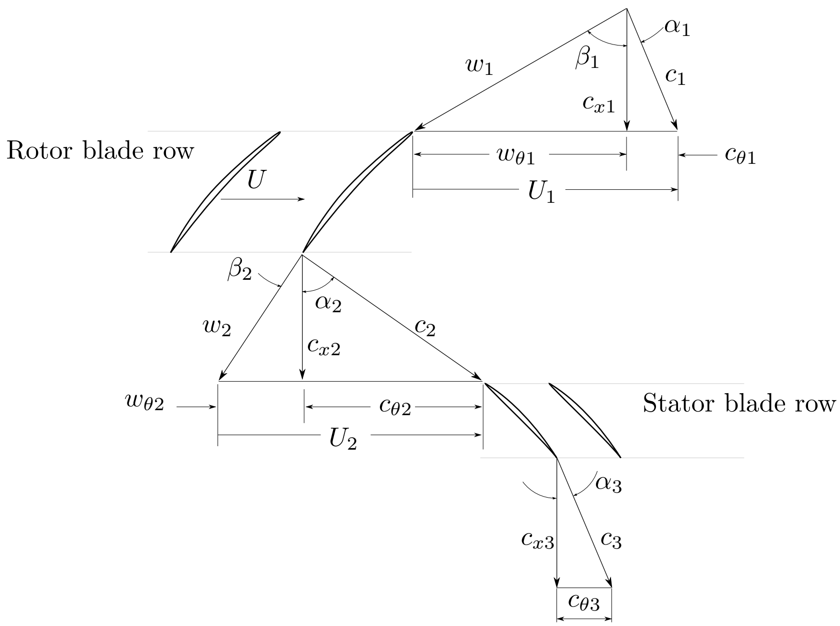

Figure 3.8: *Velocity diagram for a compressor stage*

Some of the parameters will be used in connection to numerical procedures to optimize the compressor design. These parameters are the number of stages, stage loading, degree of reaction, and geometry. Other parameters, i.e the relative tip Mach number, the axial inlet Mach number, the aspect ratio, and the ratio of clearance over chord, are selected on the basis of available empirical data and past design experience.

3.1.1 Empirical Models

This section introduces the empirical models used in the mean-line code. The nomenclature for cascades used in the models is shown in Figure 3.9.

McKenzie [56]

McKenzie noted that for 50% reaction designs, the blade stagger angle (ζ), appeared to determine the flow coefficient for the maximum stage efficiency. This was interpreted as a relationship between the stagger angle and vector mean flow angle β_m. The relationship was found to be relatively independent of the reaction. The relationship is expressed by Equation 3.6, where $\tan\beta_m = 0.5(\tan\beta_1 + \tan\beta_2)$ by definition.

$$\tan\beta_m = \tan\zeta + 0.213 \tag{3.6}$$

McKenzie proposed an alternative design rule for blades with a low stagger angle since it was noted that the peak efficiency for compressors that have blades with

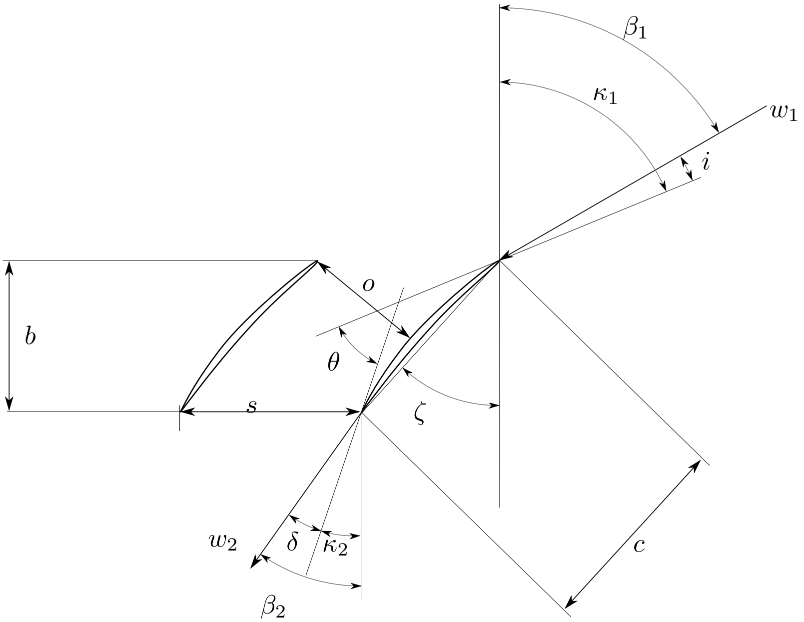

Figure 3.9: *Nomenclature for cascade*

a low stagger angle occurs close to stall. Equation 3.7 gives the new design rule that provides a larger stall margin for the compressor.

$$\tan\beta_m = \tan\zeta + 0.15 \tag{3.7}$$

The camber angle can be computed, since the blades are double circular arc blades, using the inlet flow angle and the stagger angle

$$\theta = 2(\beta_1 - \zeta)\,. \tag{3.8}$$

Wright and Miller [57]

Wright and Miller [57] introduced a model to estimate the losses, deviation, and incidence angles at the design conditions. The losses that the model takes into account are the profile losses and the endwall losses. The model also estimates the deviation at the design condition and the minimum loss incidence angle.

The first part in the profile loss model uses a correlation to calculate the equivalent diffusion ratio from the aerodynamic inlet and exit conditions, the blade spacing to chord ratio, and the thickness to chord ratio

$$D_{eq} = \left(1 - \frac{w_2}{w_1} + \left(0.1 + \frac{t}{c}\left(10.116 - 34.15\frac{t}{c}\right)\right)\frac{s}{c}\,\frac{w_{\theta 1} - w_{\theta 2}}{w_1}\right)\frac{w_1}{w_2} + 1.0\,. \tag{3.9}$$

The second part in the profile loss model relates the Lieblein loss parameter to the equivalent diffusion ratio and inlet Mach number, as shown Figure 3.10. The

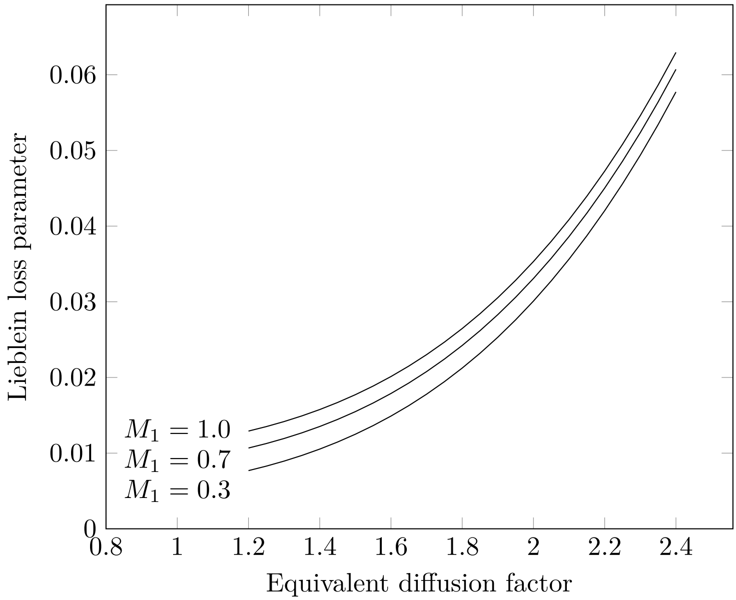

Figure 3.10: *Correlation for profile loss coefficient [57]*

definition of the Lieblein loss parameter is

$$0.5\,\omega_p\,\frac{s}{c}\left(\frac{w_1}{w_2}\right)^2\cos\beta_2\,. \tag{3.10}$$

The empirical model for the profiles loss is

$$0.5\,\omega_p\,\frac{s}{c}\left(\frac{w_1}{w_2}\right)^2\cos\beta_2 = 0.002112 + 0.007465\,M_1 + 0.001609\,D_{eq}^4\,. \tag{3.11}$$

The model for endwall losses comes from the observed trends that, as tip clearance increases the total loss increases, while the maximum achievable loading decreases. It was also observed that the maximum achievable loading decreases with increasing aspect ratio. The correlation that is presented in [57] is

$$\omega_{ew}\frac{h}{c}\left(\frac{w_1}{w_2}\right)^2 = \mathrm{func}(\frac{\varepsilon}{c}, \mathrm{loading}) \tag{3.12}$$

where the loading in the correlation is expressed as the diffusion factor, which is computed with Equation 3.13.

$$DF = 1 - \frac{w_2}{w_1} + 0.5\frac{s}{c}\frac{w_{\theta 1} - w_{\theta 2}}{w_1} \tag{3.13}$$

The correlation for the endwall loss parameter is shown in Figure 3.11 and in Equation 3.14.

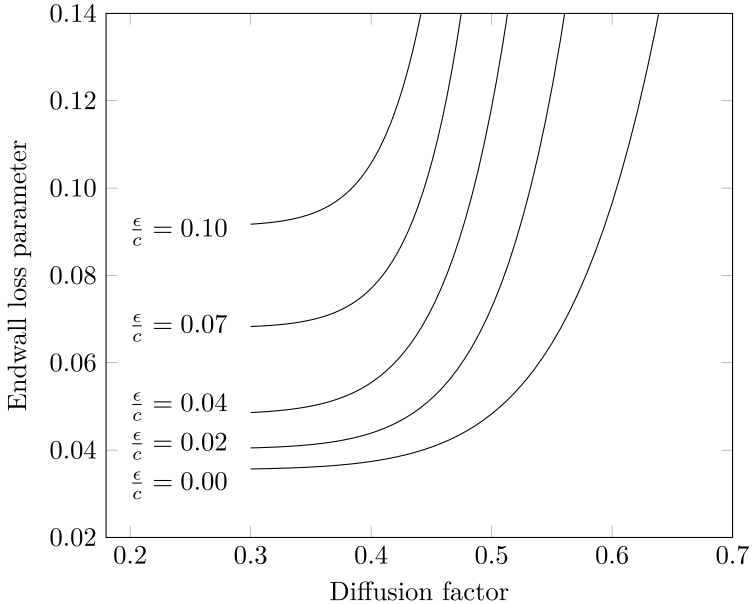

Figure 3.11: *Correlation for endwall loss coefficient [57]*

$$\text{func}(\frac{\varepsilon}{c}, \text{loading}) = \begin{cases} 4.92DF^{8.59} + 0.0355 & \text{if } \frac{\epsilon}{c} = 0.00 \\ 29.4DF^{9.82} + 0.0403 & \text{if } \frac{\epsilon}{c} = 0.02 \\ 81.9DF^{10.2} + 0.0482 & \text{if } \frac{\epsilon}{c} = 0.04 \\ 6.04 \cdot 10^{2}DF^{12.1} + 0.0680 & \text{if } \frac{\epsilon}{c} = 0.07 \\ 1.22 \cdot 10^{3}DF^{12.4} + 0.0913 & \text{if } \frac{\epsilon}{c} = 0.10 \end{cases} \tag{3.14}$$

The losses that the model estimates are assumed to be at Reynolds number of 10^6. The losses must be adjusted for the effect of Reynolds number. The correction assumes that the change in loss with Reynolds number in the laminar region follows the Blasius power law for the effect of Reynolds number on the drag of a flat plate. In the region where the Reynolds number is between 10^5 and 10^6 the change in loss with Reynolds number is comparable to the Prandtl equation for the skin friction of a flat plate in a hydraulically smooth turbulent flow. When the flow is fully turbulent it is assumed to be hydraulically rough, and there are no effects from the Reynolds number. The losses are then assumed to be constant. The correction factors are expressed in Equation 3.15 and shown in Figure 3.12.

$$\frac{\omega}{\omega_{Re=10^6}} = \begin{cases} 489.8Re^{-0.5} & \text{if } Re < 10^5 \\ 13.8Re^{-0.19} & \text{if } 10^5 < Re < 10^6 \\ 1.0 & \text{if } Re > 10^6 \end{cases} \tag{3.15}$$

The correlations estimate a loss coefficient for each loss. The coefficient for

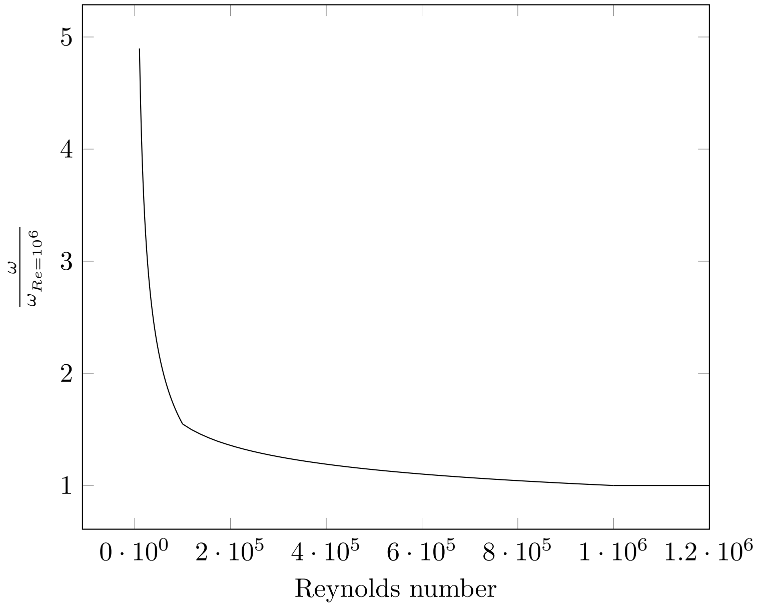

Figure 3.12: *Correlation for the effect of Reynolds number on the total losses*

the rotor is defined as

$$\omega_{\text{rotor}} = \frac{p_{01,rel} - p_{02,rel}}{p_{01,rel} - p_1} \tag{3.16}$$

and it is defined for the stator as

$$\omega_{\text{stator}} = \frac{p_{02} - p_{03}}{p_{02} - p_2}\,. \tag{3.17}$$

The correlation for minimum loss incidence that Wright and Miller derived relates the minimum loss incidence to the ratio of the throat width to the inlet spacing and the inlet Mach number.

$$\frac{o}{s\cos\beta_{1ml}} = 0.155M_1 + 0.935 \tag{3.18}$$

The correlation proposed by Wright and Miller to calculate the deviation angle is a modified form of the Carter's rule. Carter's rule states that the deviation angle is a function of the camber angle and the space chord ratio ($\delta = m\theta\sqrt{\frac{s}{c}}$). The new correlation takes into account the thickness chord ratio and the axial velocity density ratio. The correlation is

$$\delta = 1.13m\left(\theta\sqrt{\frac{s}{c}} + 3.0\right) + m_1\left(\frac{\rho_1 c_{x1}}{\rho_2 c_{x2}} - 1.0\right) + m_2\left(\frac{t}{c} - 0.05\right) + 0.8 \tag{3.19}$$

where the coefficients used in the correlation are shown in Figure 3.13 and expressed in Equations 3.20 to 3.22.

$$m = 0.2263 - 7.884\cdot 10^{-4}\,\zeta + 1.119\cdot 10^{-4}\,\zeta^2 - 1.787\cdot 10^{-6}\,\zeta^3 + 1.318\cdot 10^{-8}\,\zeta^4 \tag{3.20}$$

$$m_1 = 1.426 + 0.4464\,\zeta \tag{3.21}$$

$$m_2 = 0.8968 + 3.4041\,\zeta - 3.32\cdot 10^{-2}\,\zeta^2 - 4.2634\cdot 10^{-4}\,\zeta^3 + 2.9461\cdot 10^{-6}\,\zeta^4 \tag{3.22}$$

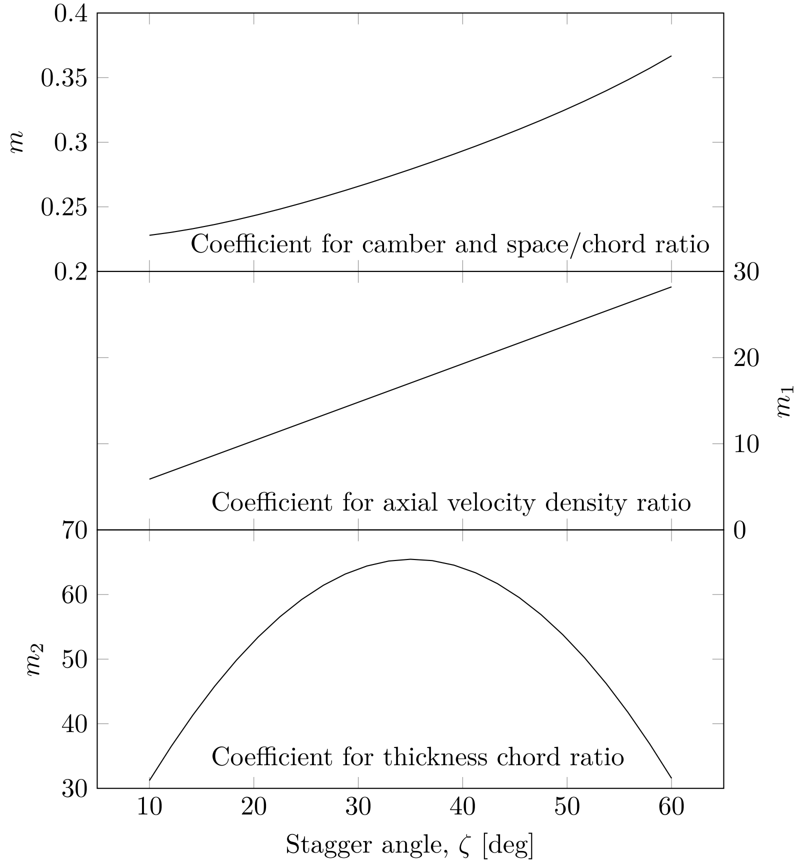

Figure 3.13: *Coefficients for the deviation correlation at optimum incidence [57]*

Schwenk [58]

The shocks encountered in transonic compressor rotors consist of a bow shock and a passage shock. A schematic of the shock wave configuration is shown in Figure 3.14. Operation conditions control the shape and location of the shocks. Schwenk proposed a model to estimate the passage shock losses at maximum compressor efficiency. The model calculates the average of the peak suction surface

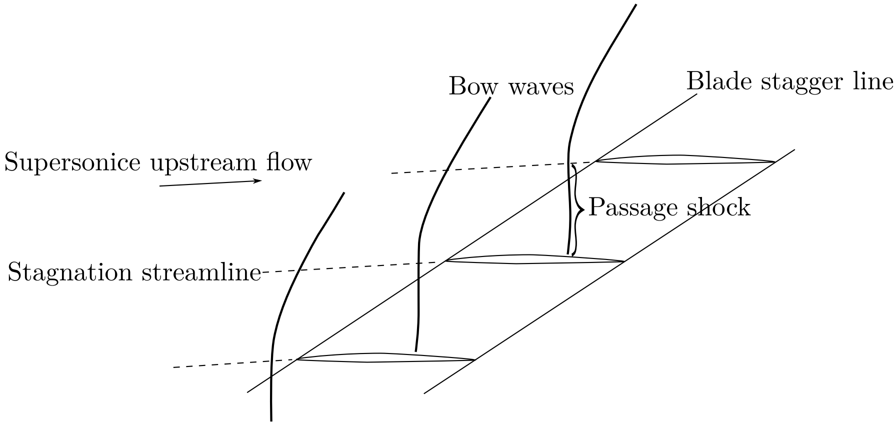

Figure 3.14: *Shock-wave configuration in cascade of airfoils at supersonic inlet relative Mach number. Reproduced from [58].*

and the relative inlet Mach number. The Prandtl-Meyer expansion equation was used to compute the peak suction surface Mach number.

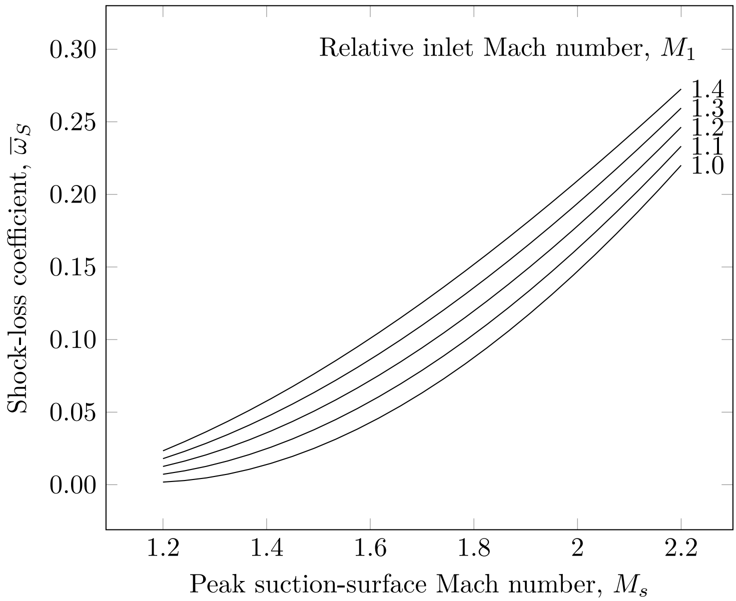

Figure 3.15: *Computed shock loss variation with peak-suction surface Mach number [58]*

$$\begin{aligned}\overline{\omega}_S = 1.049 - 1.557M_s - 0.7008M_1 + 0.5609M_s^2 \\ + 0.9296M_sM_1 - 0.02347M_s^3 - 0.2506M_s^2M_1\end{aligned} \tag{3.23}$$

NASA SP-36 [59]

The NASA SP-36 is an extensive publication that reported the state of the art aerodynamic design procedure for axial-flow compressors at that time [59]. Some of the methods and empirical correlations reported are still in use today, since new correlations that have been produced by the industry are proprietary and can not be found in the open literature. The correlations for the reference minimum-loss incidence and for the reference deviation have been used in this thesis.

The correlation for the reference minimum-loss incidence angle is

$$i_{\mathrm{ref}} = i_0 + n\,\theta \tag{3.24}$$

where i_0 is the incidence angle for zero camber angle and n is the slope of the incidence-angle variation. The correlation can be used for both circular-arc blades and NACA-65 blades. The correlation for the slope factor, n, is shown in Figure 3.16 and in Equation 3.25.

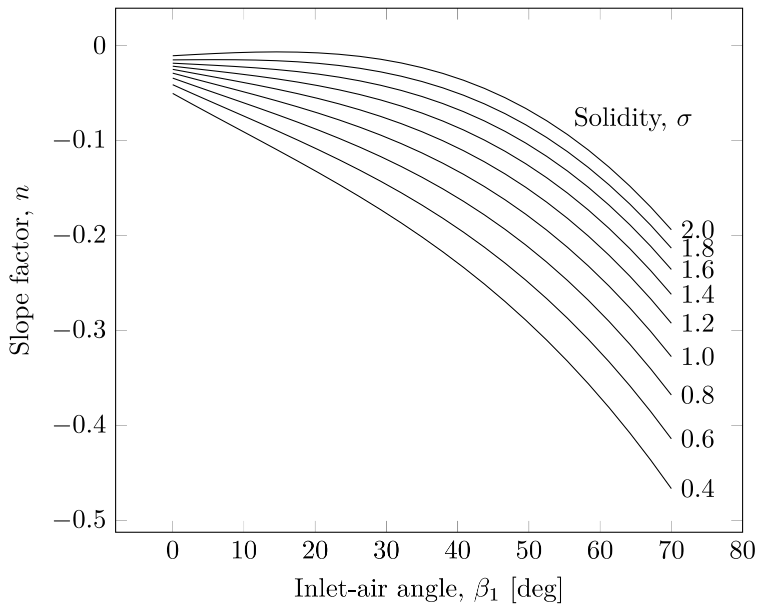

Figure 3.16: *Reference minimum-loss incidence angle slope factor deduced from low speed cascade data for NACA-65-(A_{10})-series blades as equivalent circular arcs [59]*

$$\begin{aligned} n = -0.07767 &- 5.895\cdot 10^{-3}\,\beta_1 + 2.13\cdot 10^{-5}\,\beta_1^2 - 6.016\cdot 10^{-7}\,\beta_1^3 \\ &+ 8.487\cdot 10^{-2}\,\sigma - 4.72\cdot 10^{-2}\,\sigma^2 + 1.072\cdot 10^{-2}\,\sigma^3 \\ &+ 4.604\cdot 10^{-3}\,\beta_1\,\sigma - 1.133\cdot 10^{-5}\,\beta_1^2\,\sigma - 7.216\cdot 10^{-4}\,\beta_1\,\sigma^2 \end{aligned} \tag{3.25}$$

The correlation for the incidence angle when the camber is zero is

$$i_0 = (K_i)_{sh}(K_i)_t(i_0)_{10} \tag{3.26}$$

where $(i_0)_{10}$ represents the variation of zero-camber incidence angle for the 10%-thick 65-series thickness distribution, $(K_i)_t$ is the correction necessary for maximum blade thickness other than 10%, and $(K_i)_{sh}$ is the correction necessary for a blade shape with a thickness distribution different from that of the 65-series blades. The correlation for the zero camber incidence angle for the 10% thick 65-series thickness distribution is

$$\begin{aligned}(i_0)_{10} = -0.06486 &+ 2.236 \cdot 10^{-2}\,\beta_1 + 5.174 \cdot 10^{-2}\,\sigma \\ &- 1.346 \cdot 10^{-3}\,\beta_1^2 + 6.611 \cdot 10^{-2}\,\beta_1\,\sigma \\ &+ 2.577 \cdot 10^{-5}\,\beta_1^3 + 6.222 \cdot 10^{-4}\,\beta_1^2\,\sigma \\ &- 1.619 \cdot 10^{-7}\,\beta_1^4 - 7.476 \cdot 10^{-6}\,\beta_1^3\,\sigma\end{aligned} \tag{3.27}$$

and is shown in Figure 3.17. The correction necessary for maximum blade thickness

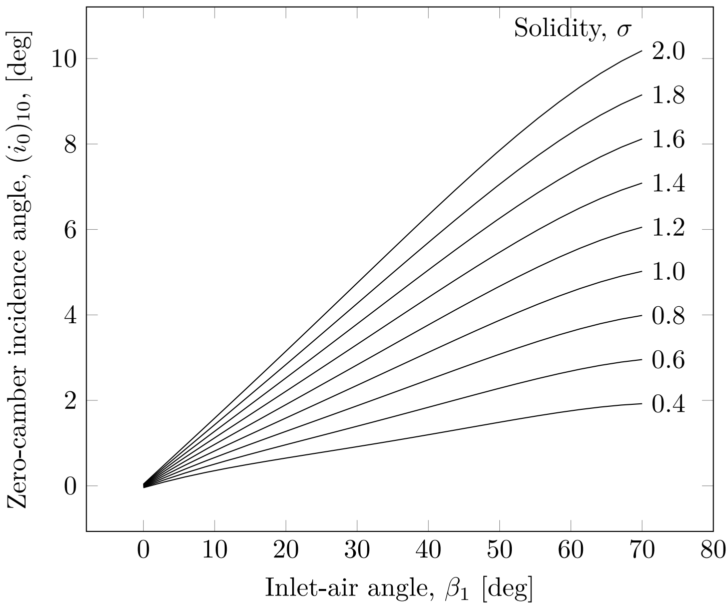

Figure 3.17: *Reference minimum-loss incidence angle for zero camber deduced from low-speed-cascade data of 10% thick NACA-65-(A_{10})-series blades [59]*

other than 10% is

$$(K_i)_t = 328.4\left(\frac{t}{c}\right)^3 - 122.5\left(\frac{t}{c}\right)^2 + 18.95\left(\frac{t}{c}\right) \tag{3.28}$$

and is shown in Figure 3.18. The correction necessary for a blade shape with a

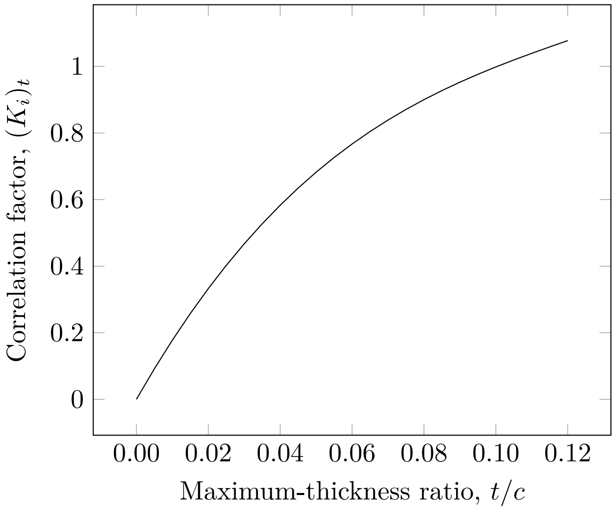

Figure 3.18: *Deduced blade maximum-thickness correction for zero-camber reference minimum-loss incidence angle [59]*

thickness distribution different from that of the 65-series blades is

$$(K_i)_{sh} = \begin{cases} 0.7 & \text{if DCA blades} \\ 1.0 & \text{if NACA 65 blades} \end{cases} \tag{3.29}$$

The correlation for the deviation is a linear variation of the reference deviation angle with a camber angle for fixed solidity and air inlet angle. The correlation is

$$\delta_{\text{ref}} = \delta_0 + m\theta \tag{3.30}$$

where δ_0 is the reference deviation angle for zero-camber, m is the slope of the deviation angle variation with camber, and ω is the camber angle. The zero-camber deviation angle correlation is

$$\delta_0 = (K_\delta)_{sh}(K_\delta)_t(\delta_0)_{10} \tag{3.31}$$

The correlation for the variation for the 10%-thick 65-series thickness distribution is

$$\begin{aligned}(\delta_0)_{10} = 0.01737 &- 1.785 \cdot 10^{-2}\,\beta_1 + 1.206 \cdot 10^{-3}\,\beta_1^2 - 2.295 \cdot 10^{-5}\,\beta_1^3 + 1.279 \cdot 10^{-7}\,\beta_1^4 \\ &- 3.102 \cdot 10^{-2}\,\sigma + 1.064 \cdot 10^{-2}\,\sigma^2 \\ &+ 3.337 \cdot 10^{-2}\,\beta_1\,\sigma - 6.689 \cdot 10^{-4}\,\beta_1^2\,\sigma + 1.164 \cdot 10^{-5}\,\beta_1^3\,\sigma \\ &- 7.147 \cdot 10^{-3}\,\beta_1\,\sigma^2 + 3.954 \cdot 10^{-5}\,\beta_1^2\,\sigma^2\end{aligned} \tag{3.32}$$

and is shown in Figure 3.19. The correction for different blade shapes is

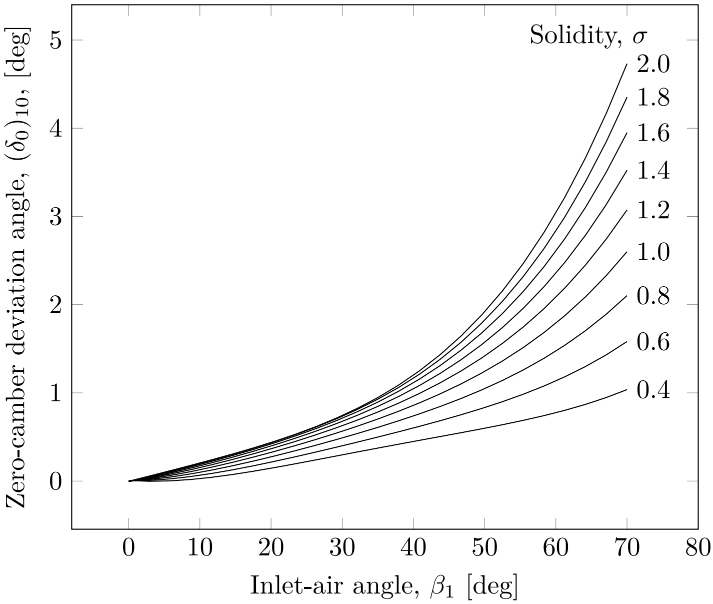

Figure 3.19: *Zero-camber deviation angle at reference minimum-loss incidence angle deduced from low-speed-cascade data for 10% thick NACA 65-($A_1$0)-series blades [59]*

$$(K_\delta)_{sh} = \begin{cases} 0.7 & \text{if DCA blades} \\ 1.0 & \text{if NACA 65 blades} \end{cases} \tag{3.33}$$

The correction necessary for maximum blade thickness other than 10% is

$$(K_\delta)_t = 6.172\frac{t}{c} + 36.61\left(\frac{t}{c}\right)^2 \tag{3.34}$$

and is shown in Figure 3.20. The impact of the solidity, σ, on the slope term, m, can be taken into account

$$m = \frac{m_{\sigma=1}}{\sigma^b} \tag{3.35}$$

where $m_{\sigma=1}$ is the value of the slope, m, at a solidity of $\sigma = 1$. The correlation for $m_{\sigma=1}$, both for DCA blades and NACA-65 blades, is

$$m_{\sigma=1} = \begin{cases} 0.249 + 7.40 \cdot 10^{-4}\beta_1 - 1.32 \cdot 10^{-5}\beta_1^2 + 3.16 \cdot 10^{-7}\,\beta_1^3 & \text{if DCA blades} \\ 0.170 - 3.33 \cdot 10^{-4}\beta_1 + 3.33 \cdot 10^{-5}\beta_1^2 & \text{if NACA 65 blades} \end{cases} \tag{3.36}$$

and is shown in Figure 3.21. The correlation for the solidity exponent is

$$b = 0.9655 - 2.538 \cdot 10^{-3}\beta_1 + 4.221 \cdot 10^{-5}\beta_1^2 - 1.3 \cdot 10^{-6}\beta_1^3 \tag{3.37}$$

and is shown in Figure 3.22.

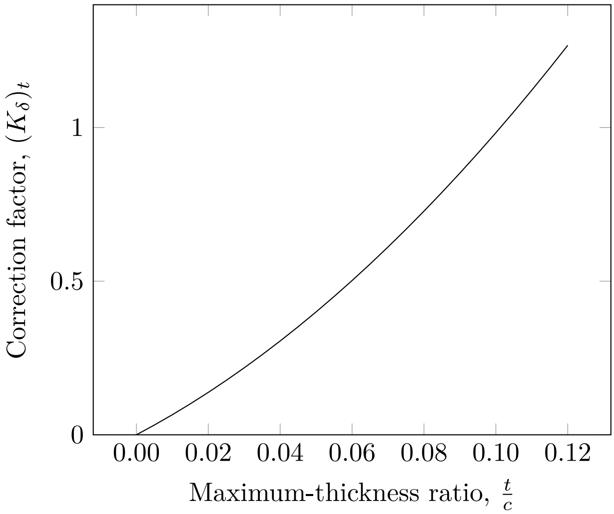

Figure 3.20: *Deduced maximum-thickness correction for zero-camber reference minimum-loss deviation angle [59]*

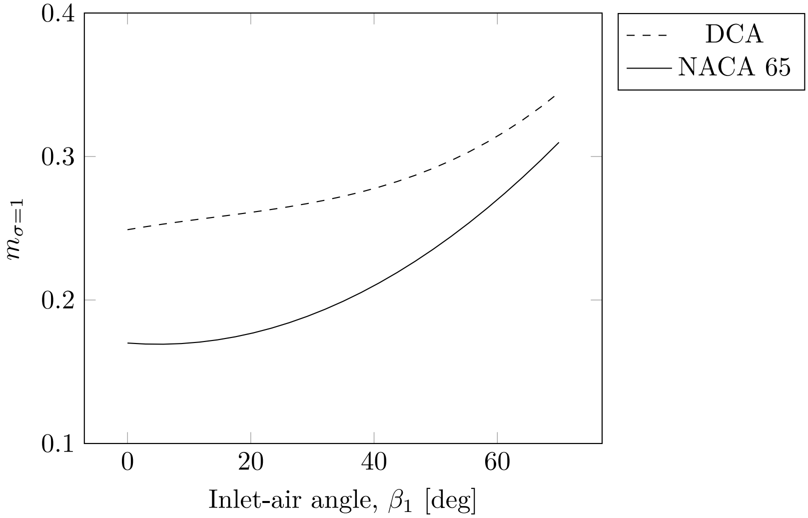

Figure 3.21: *Value of $m_{\sigma=1}$ in deviation angle rule [59]*

3.2 Two Dimensional Design

The streamline curvature approach solves the governing equations in the meridional plane, see Figure 3.23, or the blade to blade plane, or computes a coupled solution of these. However, most practical approaches solve the equations in the meridional

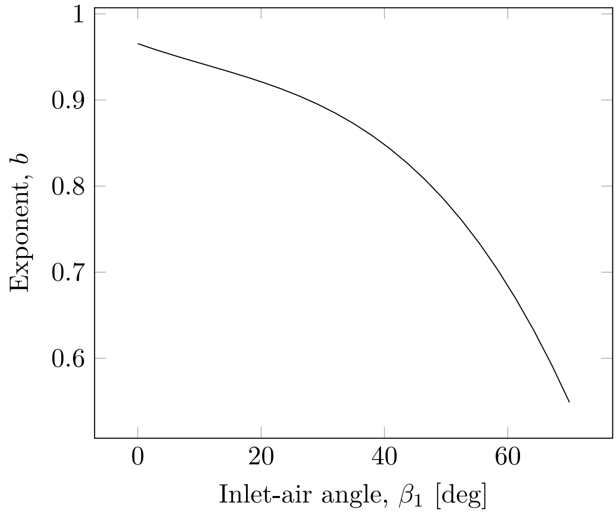

Figure 3.22: *Value of solidity exponent, b in deviation angle rule [59]*

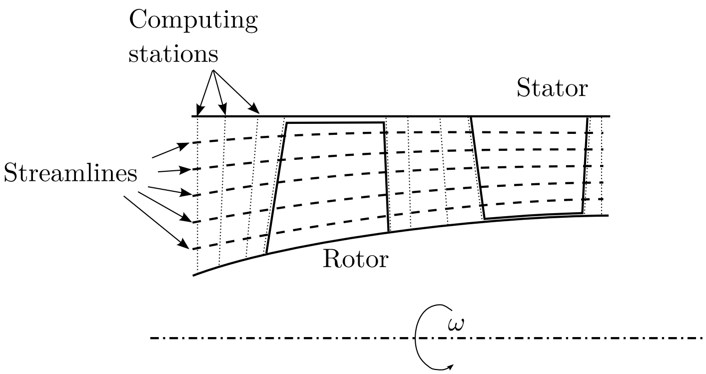

Figure 3.23: *Streamline curvatures in a compressor stage (meridional plane)*

plane. The assumptions made when using the streamline curvature approach are that the flow is steady, adiabatic, axisymmetric, and inviscid. The geometry and the nomenclature are shown in Figure 3.24. The momentum equation in the meridional direction is

$$c_m \frac{\partial c_m}{\partial m} - \frac{c_\theta^2}{r} \sin\phi = -\frac{1}{\rho}\frac{\partial p}{\partial m} + F_m\,, \tag{3.38}$$

in the stream surface normal direction

$$\frac{c_m^2}{r_c} - \frac{c_\theta^2}{r} \cos\phi = -\frac{1}{\rho}\frac{\partial p}{\partial n} + F_n\,, \tag{3.39}$$

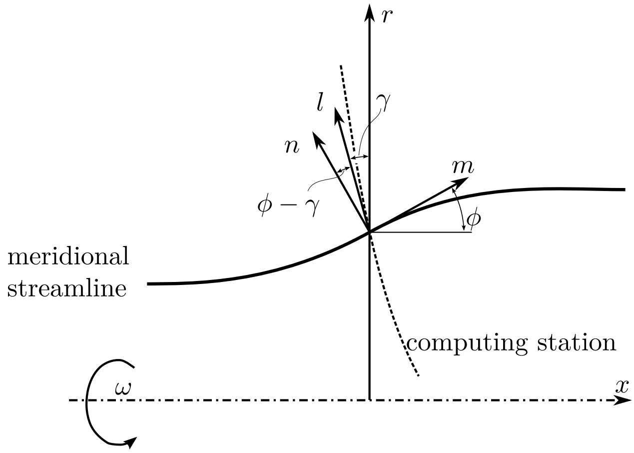

Figure 3.24: *Coordinate directions in the meridional plane*

and in the circumferential direction

$$\frac{c_m}{r}\frac{\partial(rc_\theta)}{\partial m} = F_\theta\,. \tag{3.40}$$

The energy equation for steady adiabatic flow is

$$h_0 = h + \frac{c^2}{2} \tag{3.41}$$

and the enthalpy-entropy relation is

$$\frac{1}{\rho}\mathrm{d}p = \mathrm{d}h - T\mathrm{d}s\,. \tag{3.42}$$

These equations are combined and form the radial equilibrium equation

$$\begin{aligned} c_m\frac{\partial c_m}{\partial l} =& \sin(\phi-\gamma)c_m\frac{\partial c_m}{\partial m} + \cos(\phi-\gamma)\frac{c_m^2}{r_c} - \frac{c_\theta}{r}\frac{\mathrm{d}\,(rc_\theta)}{\mathrm{d}\,l} \\ &+ \frac{\mathrm{d}\,h_0}{\mathrm{d}\,l} - T\frac{\mathrm{d}\,s}{\mathrm{d}\,l} - \sin(\phi-\gamma)F_m - \cos(\phi-\gamma)F_n\,. \end{aligned} \tag{3.43}$$

The radial equilibrium equation is the backbone of the streamline curvature method. The streamlines and computational stations for the method are shown in Figure 3.23. The streamline curvature method solves the equations for angular momentum, entropy, and radial equilibrium. The losses are taken into account using empirical correlations. The method solves the equations using an iterative procedure while satisfying the overall continuity equation. A more detailed discussion of the streamline curvature method can be found in e.g. [60–62]

The approach used in the thesis is to use a commercial program that implements the streamline curvature method [63]. The SC90C program was developed by

PCA engineers [63]. The program uses Wright and Miller for loss and deviation correlations, the same models as are used in the mean-line design program. The code also incorporates the spanwise mixing scheme from Gallimore [64, 65]. The spanwise mixing is modelled as a turbulent diffusion process. The process redistributes the losses across the span and by doing so, reduces the apparent losses near the endwalls by spreading the losses toward the mid-height. The same polynomial model is used in the program as was used in the one dimensional design code to calculate the specific heat, C_p. The model is shown in Equation 3.2, and the constants for the working fluids of the oxy-fuel combustion cycles are shown in Table 3.1.

An important design criterion for compressors is stability assessment. Compressor surge is an instability where the flow reverses and recovers at a frequency of a few cycles per second. A theory proposed by McKenzie [56] for surge is that

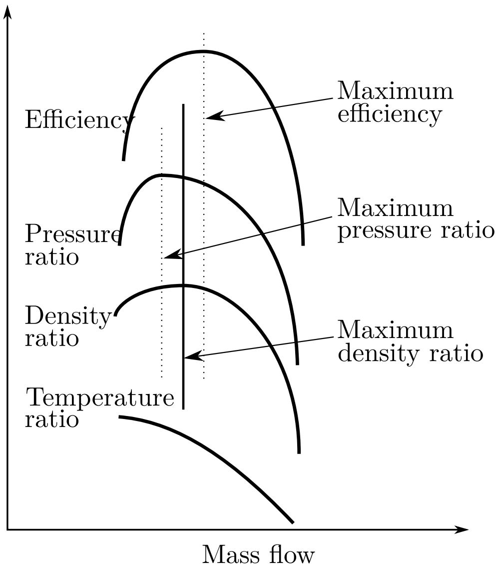

Figure 3.25: *Relative flows for maximum efficiency, pressure and density ratios [56]*

the maximum density ratio is the determining parameter for surge onset rather than the maximum pressure ratio. Figure 3.25 shows typical temperature ratio, efficiency, and pressure ratio curves as a function of mass flow when the rotation speed is held constant. It is shown in the figure that the pressure ratio is lower when the maximum efficiency occurs and the mass flow is higher.

The model built on this explanation assumes that surge will be encountered when the density ratio reaches the maximum. This model is easy to implement and tends to be more conservative than most other surge predictions. Miller and Wasdell showed that this method was in fairly good agreement with surge measurements [66].

3.3 Optimization

A number of contradicting requirements must be fulfilled to achieve a satisfactory compressor design. These requirements are e.g. high efficiency, wide operating range, high total pressure ratio per stage, low weight, and high durability [67]. The compressor design is therefore a multi-objective design problem.

The difference between a single objective optimization problem and a multi-objective formulation is that single objective problems have a unique solution, while the multi-objective has a set of compromised solutions. These are known as trade-off surfaces, Pareto optimal solutions or non-dominated solutions [68]. The meaning of these trade-off solutions is that, if all objectives are considered, then no other solutions in the search space are superior to them.

A solution to a multi-objective optimization is comprised by a number of solutions, all optimal for a particular trade between the objectives. It is therefore possible to transform the problem to a series of single objective problems with a fixed trade between the objectives. The advantage of a multi-objective solver is that it can use information from all the trade combinations simultaneously and provide a more efficient solution process.

The goal of the multi-objective optimization is to reveal the trade-off information between different objectives by finding as many Pareto optimal solutions as possible. A class of optimization methods that is particularity well suited for multi-objective formulations is evolutionary algorithms. The evolutionary algorithms are based on adaptive search techniques and mimic Darwins's theory of survival of the fittest [69]. The process most often starts from a randomly selected first generation. These are the initial values for the parameters used in the optimization scheme. The algorithm will then run the simulation and then select the next generation based on the fitness of the generation, which is selected according to the objective function values. This optimization process is the same mechanism that the natural evolution process uses, i.e. inheritance, mutation, selection, and crossover.

A multi-objective optimization environment was set up as part of this work. A one-dimensional compressor design code is used to establish a first guess on a design. An analytic mapping is then used to produce a first guess on the blade angles for a througflow solver. The throughflow solver is then interfaced with a software, iSIGHT [70], that allows multi-objective optimization. The work is described in more detail in Paper II.

4 Summary of Papers

This chapter gives a brief summary of the results reported in the six papers on which this thesis is based.

4.1 Paper I

"Conceptual Design of a Mid-Sized Semi-Closed Oxy-fuel Combustion Combined Cycle"

4.1.1 Motivation and Background

Paper I presents a conceptual design study of a semi-closed oxy-fuel combustion combined cycle. The cycle studied has a net power output of 100 MW, which is classified as a cycle in the mid-size range of the power output. Past research has concentrated on plants intended for the large power output range. The study focused on the simulation of the cycle, using the cycle simulation tool described in Section 2.1 and on the conceptual design of the gas turbine. The compressor was designed using the mean-line design tool described in Section 3.1, and the conceptual design of the turbine was accomplished using the conceptual mean-line design program LUAX-T. A single-shaft gas turbine configuration was selected for its simplicity.

The study resulted in a cycle efficiency of 47%. By considering constraints of the compressor first stage and the turbine last stage, a rotational speed of 5200 rpm was selected. An 18-stage compressor and a four stage turbine was designed for this selection.

The author and Tomas Grönstedt designed the compressor and wrote the compressor section of the paper. The author also programmed the link between IPSEpro and REFPROP. The cycle simulation and the conceptual design of the turbine were performed by Majed Sammak and Magnus Genrup. Klas Jonshagen developed components used in the cycle simulation program and Marcus Thern assisted in developing the real gas calculations.

4.2 Paper II

"Multicriteria Optimization of Conceptual Compressor Aerodynamic Design"

4.2.1 Motivation and Background

Paper II describes a design method that incorporates one dimensional and two dimensional design tools and an optimization environment. The design method aims to maximize the efficiency of the compressor while simultaneously taking the compressor stability into account through the predicted surge margin. The first step in the design method is to use a one dimensional mean-line design code to compute the boundary conditions for a two dimensional code. This is accomplished by using a simplified solution to the radial equilibrium equation to map the one dimensional results onto two dimensions. The optimization algorithm updates the boundary conditions to establish an optimal compressor design.

The method is used in a case study where a compressor is designed for an open rotor engine configuration intended for aircraft propulsion. At the time of this work, the throughflow code was not able to work with the gas mixtures present in the oxy-fuel cycles. The source code for the throughflow program was modified, and this work was reported in paper V.

The case study resulted in multiple designs that produced Pareto front of design solutions. This means that the designs are optimal in the sense that, to increase either of the objective functions, efficiency or stability, the other objective function is compromised. The value generated by this work was primarily to establish the optimization environment. This would allow future work applied to the Graz and SCOC-CC compressors.

4.3 Paper III

"Conceptual Mean-Line Design of Single and Twin-Shaft Oxy-Fuel Gas Turbine in a Semiclosed Oxy-Fuel Combustion Combined Cycle"

4.3.1 Motivation and Background

Paper III compares two different layouts, single and twin-shaft, of the gas turbine for the SCOC-CC. The paper describes the turbomachinery preliminary mean-line design of the compressor and turbine. The conceptual turbine design was performed using the mean-line design code LUAX-T, while the conceptual compressor design was accomplished using the mean-line design code described in Section 3.1.

The simulation resulted in a cycle performance of 46% net efficiency and a net output of 106 MW. The design of the single-shaft gas turbine was reported in paper A. The conceptual design of the twin-shaft gas turbine resulted in a rotational speed of 7200 rpm for the gas generation turbine and 4500 rpm for the power turbine. The gas generation turbine, which powers the compressor, was designed with two stages, while the design of the power turbine resulted in three stages. The conceptual design of the compressor resulted in a compressor with 14 stages. It was concluded from the results of this study that both single and twin-shaft oxy-fuel gas turbines have advantages. The choice of a twin-shaft gas turbine can be motivated by the smaller compressor size and the advantage of greater flexibility in operation, mainly in off-design mode. However, the advantages of a twin-shaft design must be weighed against the inherent simplicity and low cost of the simple single-shaft design.

The author was responsible for the conceptual design of the compressors and wrote the compressor part of the paper. The cycle simulation and the conceptual design of the turbine were performed by Majed Sammak and Magnus Genrup.

4.4 Paper IV

"A Comparative Analysis of Two Competing Mid-Size Oxy-Fuel Combustion Cycles"

4.4.1 Motivation and Background

Paper IV reports a study where two mid-sized oxy-fuel combustion combined cycles are compared. The two cycles are the Semi-closed Oxy-fuel Combustion Combined Cycle and the Graz cycle, which are described in Sections 2.3 and 2.4, respectively. The cycles are simulated using the simulation tool described in Section 2.1. The cycle modelling and simulation of the Graz cycle was performed by the author while this was carried out for the SCOC-CC by Majed Sammak.

The compressor design was accomplished using the mean-line design tool described in Section 3.1. The turbine design was established using the LUAX-T code from Lund University and the work was done by Majed Sammak and Magnus Genrup.

The main result of the study is that the Graz cycle is expected to achieve around a 3% higher net efficiency than the SCOC-CC. The configuration used in the SCOC-CC was to have a two-shaft configuration; in the Graz cycle, it was decided to have a geared configuration of the compressor and two turbines, one that runs the compressor and one that runs the generator. The design of the compressor for the SCOC-CC was optimized, and it was concluded that a compressor with 14 stages had a reasonably high efficiency. The conceptual design of the gas turbine for the Graz cycle resulted in a low pressure and a high pressure compressor that both have six stages. The design of the turbine part resulted in a high pressure turbine with three stages and a low pressure turbine that with four stages.

4.5 Paper V

"Integration of Fluid Thermodynamic and Transport Properties in Conceptual Turbomachinery Design"

4.5.1 Motivation and Background

Paper V presents a number of methods on how to practically include real gas thermodynamic effects into thermodynamic cycle performance programs and turbomachinery design programs. The paper describes how a streamline curvature compressor design program, a one dimensional compressor design program and a cycle performance program are linked to a thermodynamic properties program. A case study is described where the streamline curvature program is used to design a three stage compressor that has air as a working fluid. The design is completed both using a semi-perfect gas assumption and the new modification employing a state of the art real gas data thermodynamic properties program.

If not properly implemented, real gas data retrieval may completely dominate calculation times. An algorithm targeting high numerical efficiency intended for through-flow multidimensional optimization is outlined. Various implementation recommendations associated with the integration of the real gas data program into the one-dimensional compressor design program and the cycle program are described.

The author was responsible for implementing the modifications to the programs and performing the case study. Dr. Robinson provided advice regarding the modifications of the streamline curvature program. Prof. Grönstedt supervised and assisted with the writing of the paper.

4.6 Paper VI

"A Thermodynamic Analysis of Two Competing Mid-Sized Oxy-Fuel Combustion Combined Cycles"

4.6.1 Motivation and Background

Paper VI is similar to paper IV as it reports a comparison of the two oxy-fuel combustion combined cycles that have been discussed in this thesis: the Semi Closed Oxy-fuel Combustion Combined Cycle (SCOC-CC) and the Graz cycle. However, this paper goes into greater detail on the thermodynamic performance of the two cycles. Further, a reference cycle was established as the basis for the analysis of the oxy-fuel combustion cycles. A parametric study was conducted where the pressure ratio and the turbine entry temperature were varied. The optimum net efficiency for the reference cycle is 56% at a pressure ratio of 26.2 and turbine entry temperature of 1400°C. The optimum net efficiency for the SCOC-CC was 46% at a pressure ratio of 57.3 and a turbine entry temperature of 1450°C. The optimum net efficiency for the Graz cycle was also 46% at a lower pressure ratio than the SCOC-CC, at 36.5, for the same turbine entry temperature of 1450°C. The main reduction in efficiency for the oxy-fuel combustion cycles comes from O_2 production and compression. The layout and the design of the SCOC-CC is considerably simpler than in the Graz cycle while achieving the same net efficiency. The fact that the efficiencies of the two cycles are close to identical differentiates the study from previously reported work. Earlier studies have reported around a 3% advantage in efficiency for the Graz cycle, which is attributed to the use of a second bottoming cycle. This additional feature is omitted to make the two cycles more comparable in terms of complexity. Even in its simplified form, the Graz cycle requires the use of intercooling and steam cooling, in contrast to the SCOC-CC. However, the Graz cycle has a substantially lower pressure ratio at the optimum efficiency and a much higher power density for the gas turbine than both the reference cycle and the SCOC-CC.

The author did all of the simulations and analyses of the cycles and Prof. Grönstedt supervised and provided assistance with the writing of the paper.

5 Concluding Remarks

The main goals of this work have been to compare two oxy-fuel combustion combined cycles, the SCOC-CC and the Graz cycle, and to study the conceptual design of the turbomachinery for these cycles. A conventional cycle was simulated to establish a reference for the comparison of the two oxy-fuel combustion combined cycles. The reference cycle net efficiency was 56%. The reference cycle was used as a starting point for the modelling of the two cycles.

The SCOC-CC bottoming cycle has the same design as the bottoming cycle in the reference cycle, while the working fluid of the gas turbine is nearly 90% CO_2. The net efficiency for the SCOC-CC was 46.16%, although at a much higher pressure ratio than the optimal pressure ratio in the reference cycle. The optimal pressure ratio for the SCOC-CC is around 57, while it is 26 for the reference cycle. The dependency of the net efficiency on the pressure ratio is quite weak, however. At a pressure ratio of 30, the net efficiency is 45.6%. The lower pressure ratio would aid the compressor design substantially.

The standard Graz cycle is an advanced oxy-fuel combustion combined cycle that incorporates a gas turbine with steam cooling and two bottoming cycles. One of the bottoming cycles is a conventional steam cycle, while the other is a sub-atmospheric steam cycle that utilizes the heat from the flue gas condensers. The Graz cycle without the second bottoming cycle was modelled, which can be described as a simplified version and is, as such, more comparable to the layout of both a conventional combined cycle and the SCOC-CC. Both versions of the Graz cycle include steam cooling in the gas turbine and need to cool the compression using an intercooler. The simplified version of the Graz cycle reached 46.16% efficiency, while the more advanced version, the standard Graz cycle, reached 48% net efficiency. One of the benefits of the Graz cycle is the low power density of the gas turbine. This results in smaller turbomachinery for the gas turbine in the Graz cycle, which reduces the cost of this machinery. It was concluded that, for the advanced layout of the Graz cycle, the compressor needed to be a geared configuration.

It was concluded that a twin-shaft gas turbine offered more flexibility in operation and that the higher rotational speed would facilitate the compressor design and result in fewer stages for the compressor. It was further concluded that the first stage of the power turbine, both for the Graz cycle and the SCOC-CC, needs to be cooled.

References

[1] M. Sammak, K. Jonshagen, M. Thern, M. Genrup, E. Thorbergsson, and T. Grönstedt. Conceptual Design of a Mid-Sized Semi-Closed Oxy-fuel Combustion Combined Cycle. *ASME Turbo Expo 2011: Power for Land, Sea and Air, 6-10 June* (2011).

[2] E. Thorbergsson and T. Grönstedt. Multicriteria Optimization of Conceptual Compressor Aerodynamic Design. *20th International Society for Airbreathing Engines* (2011).

[3] M. Sammak, E. Thorbergsson, T. Grönstedt, and M. Genrup. Conceptual Mean-Line Design of Single and Twin-Shaft Oxy-Fuel Gas Turbine in a Semiclosed Oxy-Fuel Combustion Combined Cycle. *Journal of Engineering for Gas Turbines and Power* 135.8 (2013), 081502.

[4] E. Thorbergsson, T. Grönstedt, M. Sammak, and M. Genrup. A Comparative Analysis of Two Competing Mid-Size Oxy-Fuel Combustion Cycles. *ASME Turbo Expo 2012: Power for Land, Sea and Air, 11-15 June* (2012).

[5] E. Thorbergsson, T. Grönstedt, and C. Robinson. “Integration of Fluid Thermodynamic and Transport Properties in Conceptual Turbomachinery Design”. *Proceedings of ASME Turbo Expo 2013: Power for Land, Sea and Air. San Antonio, USA*. GT2013-95833. American Society of Mechanical Engineers. 2013.

[6] E. Thorbergsson and T. Grönstedt. A Thermodynamic Analysis of Two Competing Mid-Sized Oxy-Fuel Combustion Combined Cycles. *International Journal of Greenhouse Gas Control* (Under Review).

[7] C. Järpner, A. Movaghar, E. Thorbergsson, and T. Grönstedt. “An assessment of cooled air cooling for combined cycle gas turbines”. *5th International Conference on Applied Energy*. 2013.

[8] British Petroleum Company. *Statistical Review of World Energy 2014*. British Petroleum Co., 2014.

[9] O. Edenhofer et al., eds. *IPCC, 2014: Climate Change 2014: Mitigation of Climate Change. Contribution of Working Group III to the Fifth Assessment Report of the Intergovernmental Panel on Climate Change*. Cambridge, United Kingdom and New York, NY, USA: Cambridge University Press, Cambridge, 2013.

[10] International Energy Agency. *World Energy Outlook 2012*. International Energy Agency. Paris, 2012.

[11] International Energy Agency. *Technology Roadmap: Carbon capture and storage*. International Energy Agency. Paris, 2013.

[12] O. Edenhofer, B. Knopf, T. Barker, L. Baumstark, E. Bellevrat, B. Chateau, P. Criqui, M. Isaac, A. Kitous, S. Kypreos, et al. The economics of low stabilization: model comparison of mitigation strategies and costs. *The Energy Journal* 31.1 (2010), 11–48.

[13] J. Edmonds, J. Dooley, S. Kim, S. Friedman, and M. Wise. Technology in an integrated assessment model: the potential regional deployment of carbon capture and storage in the context of global CO2 stabilization. *Human-induced Climate Change: An Interdisciplinary Assessment, M. Schlesinger, et al., Editors* (2007), 181–197.

[14] Intergovernmental Panel on Climate Change. *Climate Change 2007 - Mitigation of Climate Change: Working Group III Contribution to the Fourth Assessment Report of the IPCC*. Cambridge, United Kingdom and New York, NY, USA: Cambridge University Press, Cambridge, 2007.

[15] B. Metz, O. Davidson, H. Coninck, M. Loos, and L. Meyer, eds. *IPCC special report on carbon dioxide capture and storage*. Cambridge University Press, 2005.

[16] M. Kanniche, R. Gros-Bonnivard, P. Jaud, J. Valle-Marcos, J. M. Amann, and C. Bouallou. Pre-combustion, post-combustion and oxy-combustion in thermal power plant for CO_2 capture. *Applied Thermal Engineering* 30.1 (2010), 53–62.

[17] M. C. Romano, P. Chiesa, and G. Lozza. Pre-combustion CO_2 capture from natural gas power plants, with ATR and MDEA processes. *International Journal of Greenhouse Gas Control* 4.5 (2010), 785–797.

[18] Siemens. *Trail-blazing power plant technology*. Retreived February, 2012. URL: `http://www.siemens.com/press/pi/EFP201105064e`.

[19] M. Sammak. "Conceptual Design of Semi-Closed Oxy-Fuel Combustion Combind-Cycle". eng. PhD thesis. Lund University, 2015, p. 175. ISBN: 978-91-7623-201-9.

[20] O. Bolland and S. Saether. New concepts for natural gas fired power plants which simplify the recovery of carbon dioxide. *Energy Conversion and Management* 33.5 (1992), 467–475.

[21] H. Jericha, W. Sanz, and E. Göttlich. Design concept for large output graz cycle gas turbines. *Journal of Engineering for Gas Turbines and Power* 130.1 (2008), 011701. DOI: `10.1115/1.2747260`. URL: `http://dx.doi.org/10.1115/1.2747260`.

[22] H. Jericha, W. Sanz, and E. Göttlich. Gas Turbine With CO2 Retention–400 MW Oxy-Fuel System Graz Cycle. *CIMAC Paper* (2007).

[23] H. Jericha, W. Sanz, E. Göttlich, and F. Neumayer. Design details of a 600 MW graz cycle thermal power plant for CO2 capture. *ASME Turbo Expo 2008: Power for Land, Sea and Air, 9-13 June* (2008).

[24] O. Bolland, H. M. Kvamsdal, and J. C. Boden. "A thermodynamic comparison of the oxy-fuel power cycles water-cycle, graz-cycle and matiant-cycle". *Power generation and sustainable development. International conference.* 2001, pp. 293–298.

[25] A. Celano. "Comparison of near Zero CO2 Emission Power Plants on CO2/H2O Mixture". PhD thesis. University of Padua, 2002.

[26] F. Franco, T. Mina, G. Woolatt, M. Rost, and O. Bolland. "Characteristics of Cycle Components for CO2 Capture". *Proceedings of 8th International Conference on Greenhouse Gas Control Technologies, Trondheim, Norway.* 2006.

[27] G. Woollatt and F. Franco. Natural gas oxy-fuel cycles–Part 1: Conceptual aerodynamic design of turbo-machinery components. *Energy Procedia* 1.1 (2009), 573–580.

[28] W. Sanz, H. Jericha, B. Bauer, and E. Göttlich. Qualitative and Quantitative Comparison of Two Promising Oxy-Fuel Power Cycles for CO Capture. *Journal of Engineering for Gas Turbines and Power* 130.3 (2008), 031702. DOI: 10.1115/1.2800350. URL: http://dx.doi.org/10.1115/1.2800350.

[29] K. Jordal. "Modeling and Performance of gas turbine cycles with various means of blade cooling". PhD thesis. Department of Heat and Power Engineering, Lund university, 2001.

[30] S. Technology. *User Documentation: Program Modules and Model Libraries.* IPSEpro Process Simulator. 2003.

[31] W. Wagner and A. Kruse. *Properties of water and steam: the industrial standard IAPWS-IF97 for the thermodynamic properties and supplementary equations for other properties: tables based on these equations.* Springer-Verlag, 1998.

[32] R. Span and W. Wagner. A new equation of state for carbon dioxide covering the fluid region from the triple-point temperature to 1100 K at pressures up to 800 MPa. *Journal of physical and chemical reference data* 25.6 (1996), 1509–1596.

[33] R. Span, E. W. Lemmon, R. T. Jacobsen, W. Wagner, and A. Yokozeki. A reference equation of state for the thermodynamic properties of nitrogen for temperatures from 63.151 to 1000 K and pressures to 2200 MPa. *Journal of Physical and Chemical Reference Data* 29.6 (2000), 1361–1433.

[34] C. Tegeler, R. Span, and W. Wagner. A new equation of state for argon covering the fluid region for temperatures from the melting line to 700 K at pressures up to 1000 MPa. *Journal of Physical and Chemical Reference Data* 28.3 (1999), 779–850.

[35] R. Schmidt and W. Wagner. A new form of the equation of state for pure substances and its application to oxygen. *Fluid Phase Equilibria* 19.3 (1985), 175–200.

[36] E. W. Lemmon, M. O. McLinden, and M. L. Huber. REFPROP: reference fluid thermodynamic and transport properties. *NIST Standard Reference Database* 23 (2007).

[37] R. Span. *Multiparameter equations of state: an accurate source of thermodynamic property data*. Springer, 2000.

[38] B. I. Lee and M. G. Kesler. A generalized thermodynamic correlation based on three-parameter corresponding states. *AIChE Journal* 21.3 (1975), 510–527.

[39] J. Estela-Uribe, A. D. Mendoza, and J. Trusler. Extended corresponding states model for fluids and fluid mixtures: II. Application to mixtures and natural gas systems. *Fluid phase equilibria* 216.1 (2004), 59–84.

[40] E. Lemmon and R. Jacobsen. A generalized model for the thermodynamic properties of mixtures. *International journal of thermophysics* 20.3 (1999), 825–835.

[41] G. A. Halls. Air Cooling of Turbine Blades and Vanes: An account of the history and development of gas turbine cooling. *Aircraft Engineering and Aerospace Technology* 39.8 (1967), 4–14.

[42] M. J. Holland and T. F. Thake. Rotor blade cooling in high pressure turbines. *Journal of aircraft* 17.6 (1980), 412–418.

[43] J. Conti et al. *International Energy Outlook 2011*. 2011, U.S. Energy Information Administration.

[44] R. J. Allam, V. White, N. Ivens, and M. Simmonds. The oxyfuel baseline: revamping heaters and boilers to oxyfiring by cryogenic air separation and flue gas recycle. *Carbon dioxide capture for storage in deep geologic formations* 1 (2005), 451–475.

[45] I. Pfaff and A. Kather. Comparative thermodynamic analysis and integration issues of CCS steam power plants based on oxy-combustion with cryogenic or membrane based air separation. *Energy Procedia* 1.1 (2009), 495–502.

[46] J. P. Tranier, N. Perrin, and A. Darde. "Update on advanced developments for ASU and CO2 purification units for oxy-combustion (Air Liquide, France)". *3rd Meeting of the Oxy-Fuel Combustion Network (IEAGHG International Oxy-Combustion Network)*. Yokohama Japan. 2008.

[47] A. Dahlquist, M. Genrup, M. Sjoedin, and K. Jonshagen. "Optimization of an Oxyfuel Combined Cycle Regarding Performance and Complexity Level". *Proceedings of ASME Turbo Expo 2013: Power for Land, Sea and Air. San Antonio, Texas, USA*. GT2013-94755. American Society of Mechanical Engineers. 2013.

[48] W. Traupel. *Thermische Turbomaschinen*. Springer-Verlag Berlin Heidelberg New York, 1977.

[49] F. Di Maria and K. Jordal. "Blade Cooling Model Comparison and Thermodynamic Analysis". *Proceedings of the 5th ASME/JSME Joint Thermal Engineering Conference. San Diego, USA*. AJTE99-6117. American Society of Mechanical Engineers. 1999.

[50] A. Dahlquist, M. Thern, and M. Genrup. "The influence from the working medium on the profile loss in compressor and turbine airfoils". *Proceedings of ASME Turbo Expo 2014: Power for Land, Sea and Air. Düsseldorf, Germany*. GT2014-25069. American Society of Mechanical Engineers. 2014.

[51] H. I. H. Saravanamuttoo, G. F. C. Rogers, H. Cohen, and P. V. Straznicky. *Gas turbine theory*. Sixth ed. Pearson Education, 2009.

[52] R. Kehlhofer, B. Rukes, F. Hannemann, and F. Stirnimann. *Combined-cycle gas & steam turbine power plants*. Pennwell Books, 2009.

[53] J. F. Louis. Systematic Studies of Heat Transfer and Film Cooling Effectiveness. *AGARD High Temp. Probl. in Gas Turbine Eng. 36* (1978).

[54] H. Grieb. *Verdichter für Turbo-Flugtriebwerke*. Springer, 2009.

[55] P. P. Walsh and P. Fletcher. *Gas turbine performance*. John Wiley & Sons, 2004.

[56] A. B. McKenzie. *Axial Flow Fans and Compressors: Aerodynamic Design and Performance*. Cranfield Series on Turbomachinery Technology, 1997 (Ashgate Publishing Limited).

[57] P. I. Wright and D. C. Miller. An improved compressor performance prediction model (1992).

[58] F. C. Schwenk, G. W. Lewis, and M. J. Hartmann. *A preliminary analysis of the magnitude of shock losses in transonic compressors.* NASA RM E57A30, 1957.

[59] I. A. Johnsen and R. O. Bullock. Aerodynamic Design of Axial-Flow Compressors. NASA SP-36. *NASA Special Publication* 36 (1965).

[60] N. A. Cumpsty. *Compressor Aerodynamics.* Longman Scientific & Technical, Longman Group UK, Limited Essex CM20 2JE, England, co-published in the United States with John Wiley & Sons, Inc, 1989.

[61] R. H. Aungier. *Axial-flow compressors: a strategy for aerodynamic design and analysis.* ASME PRESS, 2003.

[62] A. J. Wennerstrom. *Design of highly loaded axial-flow fans and compressors.* Concepts ETI, Inc, 2000.

[63] *SC90C - A streamline curvature program for axial compressors, Userguide.* PCA Engineers Ltd, Nettleham, Lincoln, UK. 2008.

[64] S. J. Gallimore. Spanwise Mixing in Multistage Axial Flow Compressors. *Journal of Turbomachinery* 108 (1986), 10.

[65] M. A. Howard and S. J. Gallimore. Viscous throughflow modeling for multistage compressor design. *Journal of turbomachinery* 115 (1993), 296.

[66] D. C. Miller and D. L. Wasdell. Off-design prediction of compressor blade losses. *C279/87, pgs* (1987), 249–258.

[67] S. Obayashi, D. Sasaki, and A. Oyama. Finding tradeoffs by using multiobjective optimization algorithms. *Transactions of the Japan Society for Aeronautical and Space Sciences* 47.155 (2004), 51–58.

[68] A. Oyama and M. S. Liou. Multiobjective optimization of a multi-stage compressor using evolutionary algorithm. *AIAA Paper* 3545 (2002).

[69] S. Tiwari, P. Koch, G. Fadel, and K. Deb. “AMGA: an archive-based micro genetic algorithm for multi-objective optimization”. *Proceedings of the 10th annual conference on Genetic and evolutionary computation.* ACM. 2008, pp. 729–736.

[70] *Isight User’s Guide, Version 5.0.* Engineous Software, Inc., Cary, NC, USA. 2010.